Monthly Notices of the ROYAL ASTRONOMICAL SOCIETY

MNRAS **513,** 2777–2793 (2022) https://doi.org/10.1093/mnras/stac1061
Advance Access publication 2022 April 18

The long-active afterglow of GRB 210204A: detection of the most delayed flares in a gamma-ray burst

Harsh Kumar,[1★†] Rahul Gupta,[2,3] Divita Saraogi,[1] Tomás Ahumada,[4] Igor Andreoni,[5] G.C. Anupama,[6] Amar Aryan,[2,3] Sudhanshu Barway,[6] Varun Bhalerao,[1] Poonam Chandra,[7‡] Michael W. Coughlin,[8] Dimple,[2,3] Anirban Dutta,[6] Ankur ghosh,[2] Anna Y. Q. Ho,[9,10] E. C. Kool,[11] Amit Kumar,[2,12] Michael S. Medford,[13,14] Kuntal Misra,[2] Shashi B. Pandey,[3] Daniel A. Perley,[15] Reed Riddle,[16] Amit Kumar Ror,[2] Jason M. Setiadi[17] and Yuhan Yao[16]

[1]*Physics Department, Indian Institute of Technology Bombay, Powai 400 076, India*
[2]*Aryabhatta Research Institute of Observational Sciences, Manora Peak, Nainital - 263 001, India*
[3]*Department of Physics, Deen Dayal Upadhyaya Gorakhpur University, Gorakhpur 273009, India*
[4]*Department of Astronomy, University of Maryland, College Park, MD 20742, USA*
[5]*Joint Space Science Institute: College Park, Maryland 20742, USA*
[6]*Indian Institute of Astrophysics, 2nd Block 100 Feet Rd, Koramangala, Bangalore 560 034, India*
[7]*Department of Science & Technology, India. National Centre for Radio Astrophysics, Tata Institute of Fundamental Research, Ganeshkhind, Pune 411007, India*
[8]*School of Physics and Astronomy, University of Minnesota, Minneapolis, MN 55455, USA*
[9]*Department of Astronomy, University of California, Berkeley, CA 94720, USA*
[10]*Miller Institute for Basic Research in Science, 468 Donner Lab, Berkeley, CA 94720, USA*
[11]*The Oskar Klein Centre, Department of Astronomy, Stockholm University, AlbaNova, SE-10691 Stockholm, Sweden*
[12]*School of Studies in Physics and Astrophysics, Pandit Ravishankar Shukla University, Raipur, Chhattisgarh - 492010, India*
[13]*Department of Astronomy, University of California, Berkeley, Berkeley CA 94720, USA*
[14]*Lawrence Berkeley National Laboratory, 1 Cyclotron Rd., Berkeley CA 94720, USA*
[15]*Astrophysics Research Institute, Liverpool John Moores University, IC2, Liverpool Science Park, 146 Brownlow Hill, Liverpool L3 5RF, UK*
[16]*Division of Physics, Mathematics, and Astronomy, California Institute of Technology, Pasadena, CA 91125, USA*
[17]*University of Minnesota, School of Statistics, 313 Ford Hall, 224 Church Street SE, Minneapolis, MN 55455, USA*

Accepted 2022 April 11. Received 2022 April 11; in original form 2022 March 14

ABSTRACT

We present results from extensive broadband follow-up of GRB 210204A over the period of 30 d. We detect optical flares in the afterglow at 7.6×10^5 s and 1.1×10^6 s after the burst: the most delayed flaring ever detected in a GRB afterglow. At the source redshift of 0.876, the rest-frame delay is 5.8×10^5 s (6.71 d). We investigate possible causes for this flaring and conclude that the most likely cause is a refreshed shock in the jet. The prompt emission of the GRB is within the range of typical long bursts: it shows three disjoint emission episodes, which all follow the typical GRB correlations. This suggests that GRB 210204A might not have any special properties that caused late-time flaring, and the lack of such detections for other afterglows might be resulting from the paucity of late-time observations. Systematic late-time follow-up of a larger sample of GRBs can shed more light on such afterglow behaviour. Further analysis of the GRB 210204A shows that the late-time bump in the light curve is highly unlikely due to underlying SNe at redshift (z) = 0.876 and is more likely due to the late-time flaring activity. The cause of this variability is not clearly quantifiable due to the lack of multiband data at late-time constraints by bad weather conditions. The flare of GRB 210204A is the latest flare detected to date.

Key words: methods: data analysis – gamma-ray burst: general – gamma-ray burst: individual: GRB 210204A.

1 INTRODUCTION

Long Gamma-Ray Bursts (GRBs) originate from the core collapse of massive stars (Kouveliotou et al. 1993; Kumar & Zhang 2015). The GRB emission consists of two distinct phases: the prompt emission typically observed in soft γ-rays and hard X-rays, and the afterglow, which has been detected across a wide range of wavelengths from radio to TeV band (Piran 2004; MAGIC Collaboration 2019).

GRB prompt emission is created by energy dissipation as the relativistic jet accelerates particles via either internal shocks or magnetic reconnection (Pe'er 2015). These particles typically emit a non-thermal spectrum that is often dominated by synchrotron radiation (Burgess et al. 2020; Zhang 2020). However, the detailed radiation physics of GRBs is not fully understood (Kumar & Zhang 2015). In practice, the prompt GRB spectrum is usually modelled

★ E-mail: harshkosli13@gmail.com
† LSSTC DSFP Fellow-2018
‡ Swarna Jayanti Fellow

phenomenologically as a 'Band' spectrum (Band et al. 1993). In addition, some spectra show additional features such as thermal components or multicoloured blackbody peaks (Pe'Er & Ryde 2017), inverse Compton scattered components (Derishev, Kocharovsky & Kocharovsky 2001), low energy spectral breaks (Oganesyan et al. 2018), deviation from synchrotron spectra (Daigne, Bošnjak & Dubus 2011), etc. The physical/spectral parameters of prompt emission – like the Lorentz Factor Γ, the peak energy $E_{\rm p}$, the isotropic equivalent energy $E_{\gamma,\,\rm iso}$, or the isotropic luminosity $L_{\gamma,\,\rm iso}$ – show some correlations like the Amati correlation (Amati 2006), which have been explored for understanding GRB properties as well as applying them for cosmology.

The interaction of the jet with the ambient medium gives rise to synchrotron emission, commonly known as the afterglow (Mészáros & Rees 1997; Sari, Piran & Narayan 1998; Piran 2005). The afterglow is broadband and lasts much longer than the GRB: being visible for hours to days in X-ray bands, days to weeks in optical, and weeks to months at radio wavelengths. From the first afterglow detection by *BeppoSAX* (GRB 970228; Costa et al. 1997), the understanding of afterglows has increased tremendously over the decades – with a huge boost from the *Neil Gehrels Swift Observatory* with its rapid response abilities (Gehrels et al. 2004). The afterglow emission is phenomenologically simple to model, and the flux F is often fit by a simple power law in both time and frequency, $F \propto t^{-\alpha}\nu^{-\beta}$. The temporal decay index α and spectral decay index β typically follow the $\alpha - \beta$ closure relation predicted by the forward shock model (Piran 2005; Zhang 2021). Some GRB afterglows show features that provide insights into the physics of the source: for instance, jet breaks (Rhoads 1999; Sari, Piran & Halpern 1999), supernovae in long GRBs (Galama et al. 1998; Galama et al. 1999), and flaring activity generated by various mechanisms (Burrows et al. 2005b; Falcone et al. 2007).

GRB 210204A, first reported by *Fermi Gamma-Ray Burst Monitor* (GBM), is a long GRB with multiple pulses in the prompt emission (Meegan et al. 2009). The optical afterglow was detected by the *Zwicky Transient Facility* (ZTF; Bellm 2014) and followed by multiple observatories in many wavebands. Here, we report our findings based on extensive follow-up of the source with multiple telescopes. The paper is organized as follows. In Section 2, we describe our observations and data reduction. We also list out public data from various sources that we have used in this work. Section 3 discusses the temporal and spectral characteristics of the prompt emission. In Section 4, we undertake broadband modelling of the afterglow, showing clear evidence of late-time brightening. We conclude by discussing various causes for this in Section 5 and identifying the most plausible one.

2 OBSERVATIONS AND DATA ANALYSIS

In this section, we present the prompt and afterglow observations carried out by various space and ground-based telescopes.

2.1 Prompt emission

GRB 210204A was discovered by the *Fermi* (GBM, Meegan et al. 2009) at UT 2021-02-04 06:29:25 (hereafter, T_0). The source was first localized to RA = 109.1°, Dec = 9.7° (J2000) with a statistical uncertainty of 4.0° (Fermi GBM Team 2021). The burst was also detected by *Gravitational-wave high-energy Electromagnetic Counterpart All-sky Monitor* (Li et al. 2021), *Konus*-Wind (Frederiks et al. 2021), and *AstroSat* (Waratkar et al. 2021). The source localization was refined by *BALROG* (Kunzweiler et al. 2021), and further by the Interplanetary Network by using data from *Fermi*, *Integral*, *Swift*, *Konus*-Wind, and *Mars-Odyssey*-HEND (Hurley et al. 2021).

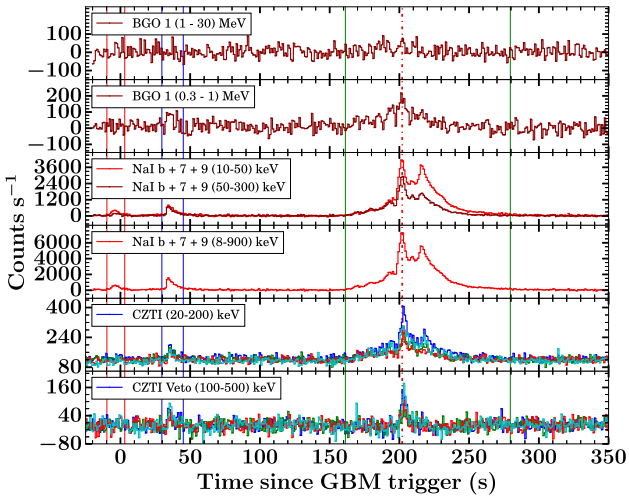

Figure 1. Top four panels: energy-resolved *Fermi*-GBM prompt emission light curves (background subtracted) of GRB 210204A. The vertical red, blue, and green lines indicate the duration of the first, second, and third episodes, respectively. The vertical dashed-dotted line indicates the peak used to calculate the isotropic luminosity of the burst. Bottom two panels: *AstroSat*-CZTI light curves in 20–200 and 100–500 keV energy range for GRB 210204A. The four colours (blue, green, red, and cyan) correspond to data from four quadrants (A, B, C, and D) of the instrument. The GRB is detected more prominently in quadrants A and D due to the location of the GRB on the sky.

In this section, we focus on the analysis of data from *Fermi* and *AstroSat* (Fig. 1).

2.1.1 Fermi-*GBM*

We retrieved the *Fermi*-GBM data (the time-tagged event mode) of GRB 210204A from the *Fermi* Science Support Center archives.[1] We performed the temporal and spectral analysis of GBM data using three sodium iodide (NaI) detectors (NaI b, NaI 7, and NaI 9) and one bismuth germanate (BGO) detector (BGO 1). These detectors have following GRB observing angles NaI b: 25° degree, NaI 7: 35° degree, NaI 9: 47°, and BGO1: 25°, respectively. For the temporal analysis of *Fermi*-GBM data, we utilized RMFIT VERSION 4.3.2 software[2] and generated the prompt emission background subtracted light curve of GRB 210204A in different energy ranges. Furthermore, we performed the spectral analysis of *Fermi*-GBM data using the Multi-Mission Maximum Likelihood framework (`3ML`[3]; Vianello et al. 2015). We performed time-integrated as well as time-resolved spectral analysis of GBM data to constrain the possible emission mechanisms of GRB 210204A. We started the spectral modelling using the traditional GRB model called `Band` or `GRB` function (Band et al. 1993). In addition to `Band` function, we explore various other possible models such as simple `power-law` model, a power-law model with a high energy spectral cutoff (`cutoffpl`), `BlackBody` function to search for photospheric signature in the spectrum, a power-law function with two sharp spectral breaks (`bkn2pow`[4]), or

[1] https://fermi.gsfc.nasa.gov/ssc/data/access/
[2] https://fermi.gsfc.nasa.gov/ssc/data/analysis/rmfit/
[3] https://threeml.readthedocs.io/en/latest/
[4] https://heasarc.gsfc.nasa.gov/xanadu/xspec/manual/node140.html

a combination of these models. We utilized the deviance information criterion (Spiegelhalter et al. 2002) to find the best-fitting model. A more detailed methodology for GBM data analysis is discussed in Gupta et al. (2021b, 2022).

2.1.2 AstroSat ***CZTI***

AstroSat Cadmium Zinc Telluride Imager (CZTI; Bhalerao et al. 2017) detected the second and third pulse of GRB 210204A, with a total of 18 141 photons: 94 per cent of which came from the brighter third pulse (Sharma et al. 2020; Waratkar et al. 2021). These two pulses were also clearly seen in the veto detectors. In detector coordinates, the GRB was incident from $\theta = 75.43$ deg and $\phi = 172.80$ deg: just 15° from the detector plane. CZTI can be used to measure the polarization of GRBs by analysing two-pixel Compton events (Chattopadhyay et al. 2014; Vadawale et al. 2015). However, such measurements are robustly possible only for GRBs with $\theta < 60$ deg (Chattopadhyay et al. 2019) – ruling out the possibility of polarimetric studies of GRB 210204A.

2.2 Multiwavelength afterglow

The large 4° positional uncertainty in the *Fermi* localization precluded prompt follow-up observations by most telescopes. However, Kool et al. (2021) used the wide-field ZTF and reported the discovery of a fast optical transient ZTF21aagwbjr/AT2021buv, a candidate afterglow for GRB 210204A∼38 min after the trigger. Subsequent follow-up observations by multiple telescopes verified the fading nature of this source and confirmed that it was indeed the afterglow of GRB 210204A.

2.2.1 X-ray afterglow

Equipped with the precise afterglow position, the *Neil Gehrels Swift Observatory* started Target-of-Opportunity observations of the GRB 210204A field about 1.6×10^5 s after the initial burst (Evans & Swift Team 2021). The *Swift X-ray telescope* (XRT; Burrows et al. 2005a) detected an uncatalogued X-ray source at RA, Dec. = 117.08071 deg, +11.40951 deg (J2000), consistent with the optical position. Multiple observations obtained till 3×10^5 s after the burst confirmed the fading nature of this source.

We used the XRT online repositories by Evans et al. (2007, 2009) to retrieve the light curves[5] and spectra,[6] respectively. We undertook spectral analysis with the XSPEC (Arnaud 1996) VERSION 12.10.1. The 0.3–10 keV spectra were modelled as a simple absorbed power law (using the `XSPEC phabs` model). For the time-averaged XRT spectrum (from $T_0+1.61 \times 10^5$ to $T_0+ 1.73 \times 10^5$ s), we get $\Gamma = 1.73^{+0.28}_{-0.26}$, and $N_H = 6.43^{+5.40}_{-4.19} \times 10^{21}$ cm^2. In Table A3, we give the temporal evolution of XRT unabsorbed fluxes and photon indices (determined from the hardness ratio) obtained from the Swift Burst Analyser web page, supported by the UK Swift Science Data Centre.

2.2.2 Optical afterglow

Kool et al. (2021) discovered the afterglow about 38 min after the initial burst. They also reported a non-detection of the same object in serendipitous observations of the field about 1.9 h prior to their first detection [see Andreoni et al. (2021) and Ho et al. (2022) for discovery details]. Follow-up observations obtained by various groups (see for instance Table A2) revealed that the source was indeed the fading afterglow of GRB 210204A and measured the source redshift. We embarked on an extensive monitoring campaign using various telescopes in the time interval between ∼0.03 and ∼20 d, after the burst event.

We discuss our observations from four Indian facilities in this section and present a summary of data reported by other groups.

We followed up GRB 210204A with the *GROWTH-India Telescope* (GIT), a 0.7 m telescope located at the Indian Astronomical Observatory, Ladakh. The telescope was equipped with a 2184 × 1472 pixel Apogee KAF3200EB camera, giving a limited 11 × 7.5 arcmin^2 field of view. While poor observing conditions prevented immediate follow-up after the announcement of the ZTF discovery, our observations began on 2021 February 6, 2.36 d after the initial alert, and continued till 2021 March 1. Typical observations consisted of multiple 300 s exposures in the r′ filter, with each exposure having a limiting magnitude of ∼20.5 mag. We used the 2.0 m *Himalayan Chandra Telescope* (HCT) on three nights: 2021 February 07, 2021 February 12, and 2021 February 14, under proposal number HCT-2021-C1-P2. Data were obtained in Bessel V, R, and I filtres (Table A1). The 3.6 m *Devasthal Optical Telescope* (DOT), located at the Devasthal Observatory of Aryabhatta Research Institute of Observational Sciences (ARIES), Nainital, India (Sagar, Kumar & Omar 2019) was triggered under our Target of Opportunity (ToO) proposal numbers DOT-2021-C1-P62 (PI: Rahul Gupta) and DOT-2021-C1-P19 (PI: Ankur Ghosh) for the follow up. We observed GRB 210204A on multiple epochs with the 4K × 4K CCD IMAGER (Pandey et al. 2018; Kumar et al. 2021). The first observations were obtained in BVRI filtres (Gupta et al. 2021c), while data on subsequent nights were obtained in the SDSS r filter. Further, we also obtained data with the 1.3 m *Devasthal Fast Optical Telescope* (DFOT) located at Devasthal observatory of ARIES, Nainital, India (Sagar et al. 2011) under our ToO Proposal ID DFOT-2021A-P6 (PI: Rahul Gupta). We obtained data in B, V, R, and I filters on 2021 June 06 (T_0+ 2.4 d), and more data in R and I bands on 2021 February 13 UT.

Data obtained from all these facilities were reduced in similar manner using a python-based reduction pipeline. Images were calibrated using bias and flat frames; pipeline made use of ASTROSCRAPPY (McCully & Tewes 2019) python package to remove cosmic rays from the science images. Once the images were corrected for all artefacts, we solved the images for astrometry using astrometry.net `solve-field` engine (Lang et al. 2010) in offline mode. Sources in images were extracted in the form of a locally generated catalogue via `SExtractor` (Bertin & Arnouts 1996). PSFEX astromatic software (Bertin 2011) gave the PSF profile of the sources, which was used to get magnitudes of stars in the images. For images obtained in *ugriz* filters, these magnitudes were cross-matched with Panoramic Survey Telescope and Rapid Response System (Pan-STARRS) DR1 catalogue (Chambers et al. 2016) and Sloan Digital Sky Survey (SDSS) DR12 catalogue (Alam et al. 2015) using VizieR to get the zero-points of the images. While, for *BVRI* filter images, we used data from SDSS (Alam et al. 2015) and converted the magnitudes to VRI bands using Lupton (2005) transformations[7] to estimate the zero-points. For later epochs, where the afterglow was fainter, multiple exposures were stacked together using `SWarp` (Bertin et al. 2002). Table A1 lists the magnitudes with 1σ uncertainties. In case the source was not detected, we report 5σ upper limits.

[5] https://www.swift.ac.uk/xrt_curves/
[6] https://www.swift.ac.uk/xrt_spectra/
[7] http://classic.sdss.org/dr4/algorithms/sdssUBVRITransform.html

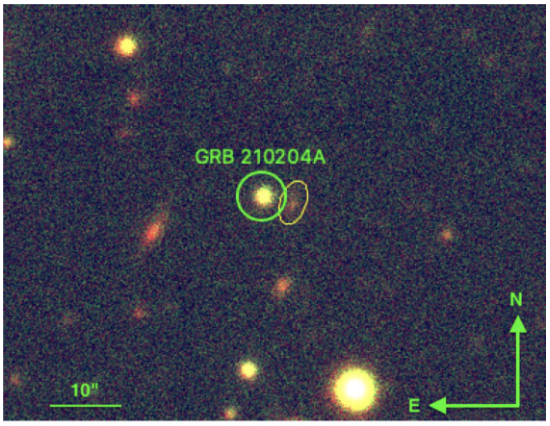

(a) DOT image of GRB

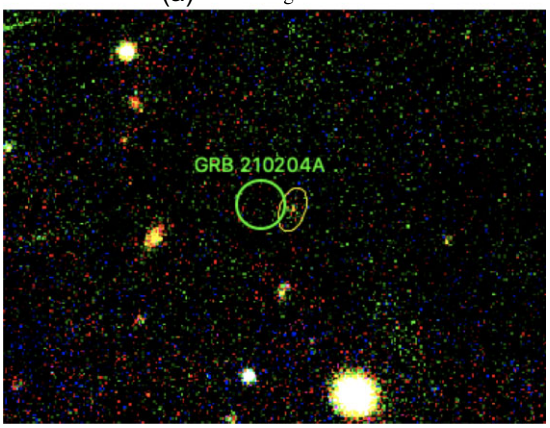

(b) Pan-STARRS DR1 image

Figure 2. GRB 210204A detection by the 4K × 4K CCD IMAGER mounted at the axial port of DOT. (a) An image of GRB 210204A afterglow detection in DOT image. The position of afterglow is indicated by the green circle. There is a galaxy present at ∼4.4 arcsec from the location of GRB (shown with a yellow ellipse), but it is unlikely to be the host (Section 2.2.2). (b) Snapshot of Pan-STARRS image of the same field is shown where no source is present at the position of afterglow.

In addition to the observations taken by our group, we also use publicly available data reported in Gamma-Ray Coordination Network (GCN) by various groups. This set includes data from the ZTF published in (Andreoni et al. 2021), 1.6-m *AZT-33IK telescope*,[8] 70-cm *AS-32 telescope* (Molotov et al. 2009), *Large Binocular Telescope* Hill (2010), 2.6-m *Shajn Telescope* (Ioannisiani, Gambovskii & Konshin 1976), and the *AZT-20* at Assy-Turgen observatory.[9] These data, along with the GCN references, are tabulated in Table A2.

Fig. 2 shows the detection of GRB afterglow with DOT (located by the green circle in the image). In DOT images, a galaxy is present ∼4.4 arcsec away from the afterglow position. This transforms to a physical distance of ∼33 kpc from GRB location, which is rather large for the galaxy to be the host of GRB 210204A. Further, the photometric redshift of this galaxy is $z_{\rm phot} = 0.436$ makes it implausible to be the host of GRB 210204A.

[8]http://en.iszf.irk.ru/Sayan_Solar_Observatory
[9]https://fai.kz/observatories/assy-turgen

2.2.3 *Spectroscopy*

We triggered a long-slit spectrum of GRB 210204A with GMOS-S under our ToO program GS-2021A-Q-124 (PI: A. Ho). The observation, conducted in the Nod-and-Shuffle mode with a 1 arcsec wide slit, started at 2021 February 06 01:19:09.2 UT, corresponding to 42.8 h after the *Fermi*-GBM trigger. We obtained 2 × 450 s spectroscopic exposures with the B600 grating and 2 × 450 s exposures with the R400 grating, providing coverage over the range 3620–9600 Å. Flux calibration was not performed. The spectrum was reduced using the IRAF package for GMOS. We identified a series of strong absorption features at $z = 0.876$ superposed on a relatively flat, featureless continuum (Fig. 3).

We also detected intervening absorption systems of Mg II λλ2796, 2803 at $z = 0.666$ and $z = 0.712$. This interpretation is consistent with that of Izzo et al. (2021), who obtained spectra using ESO VLT UT3 equipped with X-shooter spectrograph ∼1.79 d after the trigger. Their spectra spanned the wavelength range from 3000 to 21 000 Å; in which they report a few absorption lines of Al II, Ca II, Fe II, Mg I, Mg II, Zn II, Ca H, and K detected at a common redshift of z = 0.876. They also detect three intervening Mg II absorbers at redshifts of z = 0.71, 0.66, and 0.57.

2.2.4 *Radio afterglow*

The GRB 210204A event was triggered with the upgraded *Giant Metrewave Radio Telescope* (uGMRT) at 2021 February 20.56 UT in band 5 (1000–1450 MHz). The observations were 2 h in duration, including overheads using a bandwidth of 400 MHz. We use the COMMON ASTRONOMY SOFTWARE APPLICATIONS (McMullin et al. 2007) for data analysis. The data were analysed in three major steps, i.e. flagging, calibration, and imaging using the procedure laid out in Maity & Chandra (2021). A source was clearly detected at the RA(J2000) = $07^{\rm h}48^{\rm m}19^{\rm s}.34$, Dec.(J2000) = $11^{\circ}24'33''.91$. This position is consistent with the position reported by ZTF for the GRB (Kool et al. 2021). Further follow-up observations were triggered on 2021 March 07.59 UT and 2021 March 09.56 UT in the uGMRT bands 4 and 5, respectively, 2 h at each band including overheads. In both observation, the source was detected with a resolution of 2.66 × 1.74 arcsec^2 and 6.87 × 2.05 arcsec^2. Table A4 lists the detailed radio follow-up information.

3 PROMPT EMISSION

We analyse the *Fermi* data of the prompt emission to characterize GRB 210204A and compare it with the overall GRB population.

3.1 Spectral analysis of the complete GRB

The prompt emission light curve of GRB 210204A obtained using *Fermi*-GBM data shows three distinct episodes, separated by quiescent temporal gaps (see Fig. 1). The first two episodes have relatively faint and simple fast rising and exponential decay profiles, but the third and brightest episode has rich sub-structure. The T_{90}duration for the entire burst is 207.86 ± 0.06 s. The time-integrated (the entire duration of the burst) *Fermi*-GBM spectrum (from $T_0-9.73$ to $T_0+279.55$ s) could be best explained using the traditional `Band` plus `Blackbody` model with following spectral parameters: peak energy ($E_{\rm p}$) = 146 ± 14 keV, low energy spectral index $\alpha_{\rm pt} = -1.30 \pm 0.07$, high energy spectral index $\beta_{\rm pt} = -2.39^{+0.17}_{-0.18}$ and temperature $kT_{\rm BB} = 6.5 \pm 0.6$ keV.

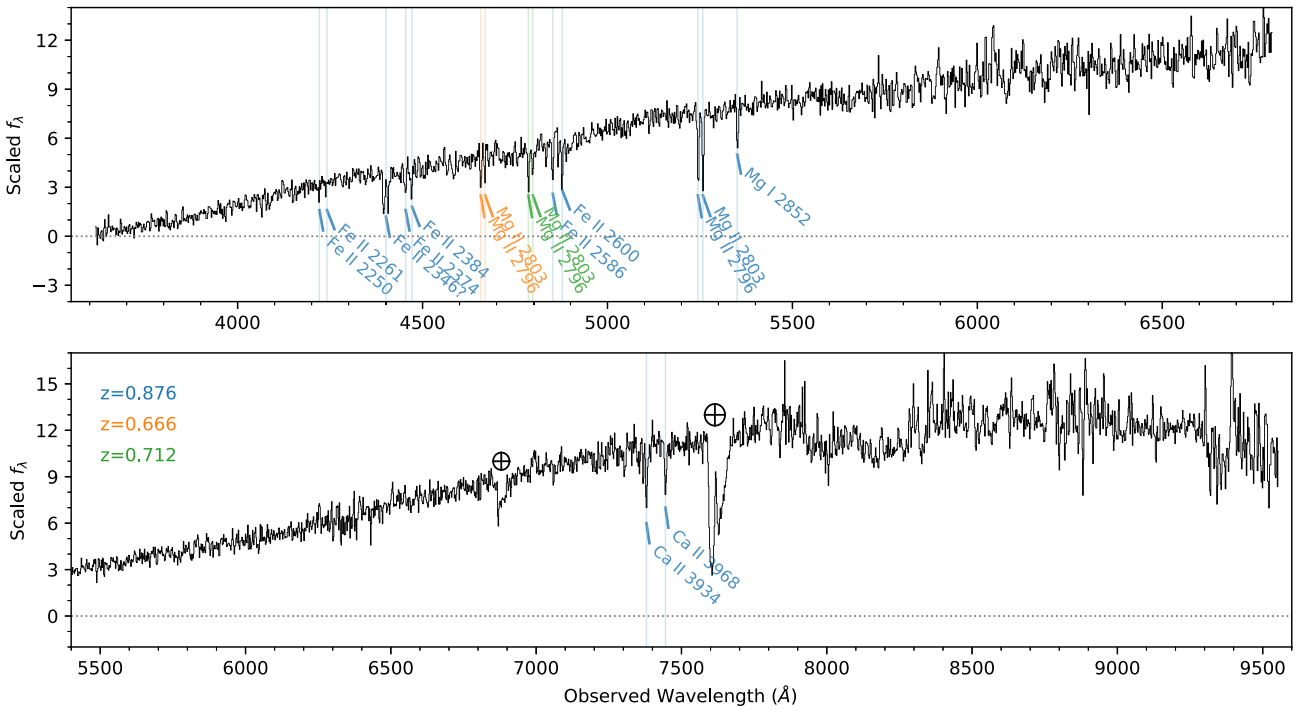

Figure 3. GMOS-S spectrum of ZTF21aagwbjr. The upper and bottom panels show the resulting spectrum in the blue and red gratings, respectively. We identify a number of strong, narrow absorption features of Fe II, Mg II, M I, and Ca II at a common redshift of $z = 0.876$ (blue notations). We identify two additional intervening absorbers, based on Mg II λλ2796, 2803 at $z = 0.666$ (orange notations) and $z = 0.712$ (green notations).

Table 1. Comparison between the characteristics of three episodes of GRB 210204A. The quiescent duration between the first two episodes is ∼26.2 s, while that between the second and third episode is ∼116.2 s. A blackbody component is needed only for the third episode (Section 3.2). All reported values are observer frame values. The total energy and luminosity were calculated using the source redshift $z = 0.876$. T_{90}: Duration in 50–300 keV band; HR: ratio of the counts in 50–300 keV to the counts in 10–50 keV; E_p, α, β: Band spectral fit parameters; F: Bolometric energy flux; $E_{\gamma,iso}$: Isotropic energy; $L_{p,iso}$: Isotropic peak luminosity.

Characteristics	Episode 1	Episode 2	Episode 3
T_{90}(s) in 50–300 keV	12.04 ± 0.02	12.81 ± 0.04	82.66 ± 0.05
HR	0.41	0.79	0.57
E_p(keV)	36 ± 9	197 ± 30	146 ± 9
α	−0.96 ± 0.36	−1.21 ± 0.07	−1.30 ± 0.04
β	−2.14 ± 0.14	−2.6 ± 0.3	−2.46 ± 0.14
kT_{BB}	···	···	6.39 ± 0.40
F (10^{-7}erg cm^{-2} s^{-1})	$1.6^{+3.65}_{-1.13}$	$3.8^{+0.9}_{-0.7}$	7.9 ± 1
$E_{\gamma,iso}$ (erg)	4.19×10^{51}	1.22×10^{52}	1.94×10^{53}
$L_{p,iso}$ (erg s^{-1})	1.80×10^{51}	4.44×10^{51}	1.70×10^{52}

3.2 Episode-wise analysis

If we analyse the three pulses separately, we see that the $E_p$values for the second and third pulses are higher (Table 1). We find that the band function gives acceptable spectral fits to the first and second episodes. The third episode is better fit by a power law with two breaks (`bkn2pow`) or by a Band spectrum with an added blackbody component. The thermal component has a temperature of 6.4 ± 0.4 keV. We use the Band + blackbody model in the rest of this section. We note that due to the lower intensity of the first two episodes, the data quality is not high enough to rule out such spectral features in them.

The presence of a thermal component, along with a non-thermal component, indicates a hybrid jet composition, including a matter-dominated hot fireball and a colder magnetic-dominated Poynting flux component for GRB 210204A. The low energy spectral index values (Table 1) are within the range expected for synchrotron emission, $-3/2 < \alpha < -2/3$.

We calculated the T_{90} values and the (50–300 keV)/(10–50 keV) hardness ratios for the entire GRB and the three episodes within it. Following Narayana Bhat et al. (2016), we estimated the errors in these by simulating 10 000 light curves by adding Poisson noise with mean equal to observed values and repeating these measurements on each simulated light curve. Fig. 4 shows these values compared to the population of long and short GRBs – we find that GRB 210204A, as well as the three individual emission episodes within it, are all consistent with the 'long–soft' GRB population.

3.3 GRB global relationships

The time-integrated rest-frame peak energy ($E_{p,i}$) of the prompt emission spectrum of GRBs is correlated to the isotropic equivalent energy ($E_{\gamma,iso}$), and this correlation is defined as Amati correlation (Amati 2006). Basak & Rao (2013) studied the episode-wise Amati correlation for a sample of *Fermi*-GBM detected GRBs with a measured redshift and confirmed that this correlation is more robust and valid for the episode-wise activity of GRBs. Recently, Chand et al. (2020) studied the Amati correlation for a sample of two-episodic GRBs and found that other than the first episode of GRB 190829A, each episode of two-episodic GRBs are consistent with the Amati correlation. In addition to GRB 190829A, a few other GRBs such as GRB 980425B, GRB 031203A, and GRB 171205 do not follow the Amati correlation.

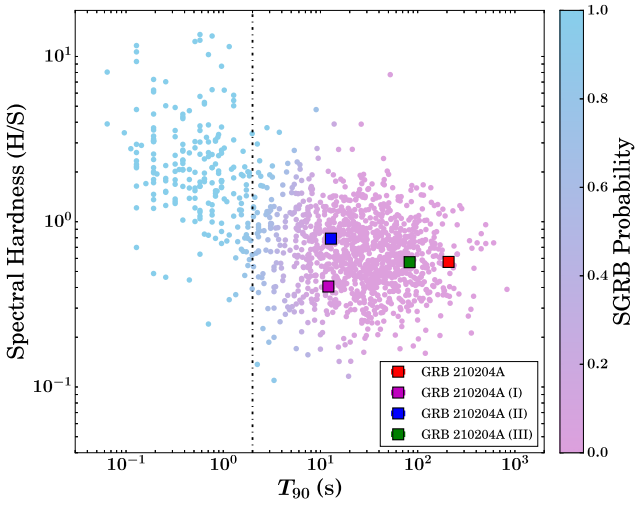

Figure 4. Prompt emission T_{90}-HR correlations: (a) time-integrated (shown with a red square), and episode-wise (shown with magenta, blue, and green squares for the first, second, and third episodes, respective) T_{90}-HR correlation for GRB 210204A. We have also shown the data points for long and short GRBs taken from Goldstein et al. (2017). The right side y-scale shows the probability of short GRBs. The vertical black dashed-dotted line indicates the boundary between two classes of GRBs.

Another variant of Amati correlation is the Yonetoku correlation, which is the correlation between time-integrated rest-frame peak energy ($E_{\rm p,\,i}$) and isotropic peak luminosity $L_{\gamma,\,\rm iso}$ (Yonetoku et al. 2004). These correlations have been utilized to classify individual episodes in GRBs with long quiescent phases. Fig. 5 shows GRB 210204A on the Amati and Yonetoku correlations. We find that the time-integrated, as well as individual episodes values, are consistent with the Amati correlation of typical long GRBs. Similarly, the $L_{\gamma,\,\rm iso}$, and $E_{\rm p,\,i}$ values for individual episodes are consistent with the Yonetoku correlation.

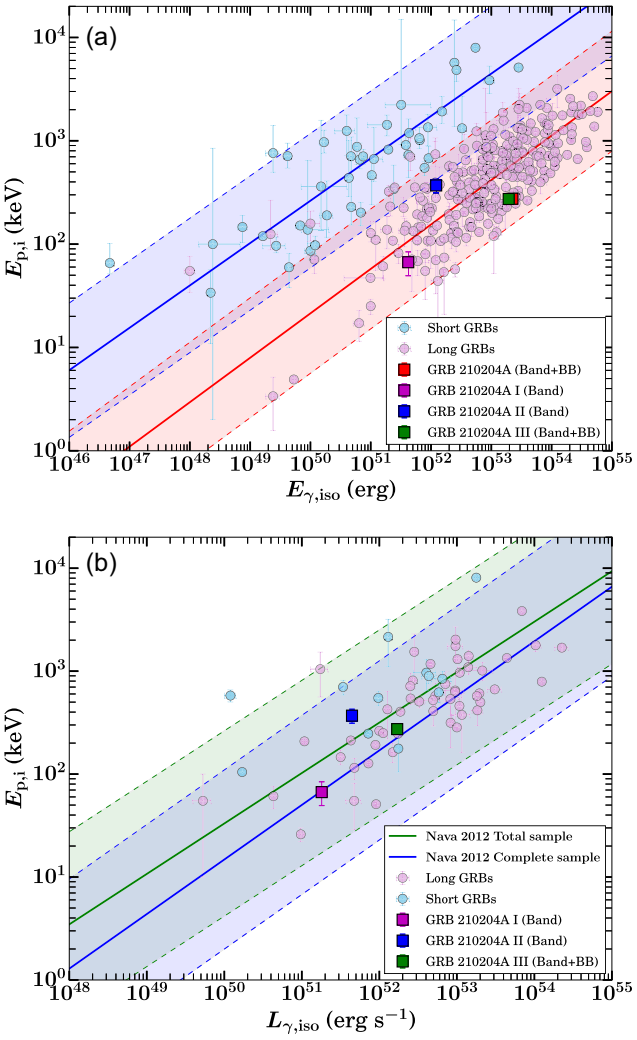

Figure 5. Prompt emission Amati and Yonetoku correlations: (a) time-integrated (shown with a red square), and episode-wise (shown with magenta, blue, and green squares for the first, second and third episodes, respective) Amati correlation for GRB 210204A. Note that the $E_{\rm p}$ values have been converted to the rest frame using the GRB redshift $z = 0.876$. We also show the data points for long and short GRBs taken from Minaev & Pozanenko (2020). The red and blue solid lines show the best-fitting line for long and short bursts, and the shaded regions represent the 2σ uncertainty region for both the populations of GRBs. (b) The episode-wise (shown with magenta, blue, and green squares for the first, second and third episodes, respective) Yonetoku correlation for GRB 210204A. We also show the data points for long and short GRBs taken from Nava et al. (2012). The green and blue solid lines show the best-fitting line, and the shaded regions represent the 3σ uncertainty region.

4 AFTERGLOW

The GRB blast-wave interacts with the circumburst medium giving rise to synchrotron emission, which is one of the primary signatures of standard GRB fireball model (Granot & Sari 2002). The electrons have a power-law energy distribution characterized by the index p, which results in the spectral energy distribution, which can be described as a series of multiple power-law segments. These segments join each other a particular frequencies known as break frequencies i.e. self absorption frequency ($\nu_{\rm sa}$), cooling frequency ($\nu_{\rm c}$), and synchrotron frequency ($\nu_{\rm m}$). In optical and X-rays emission, synchrotron self-absorption does not play an important role and hence can be neglected. Depending on the ordering of two break frequencies $\nu_{\rm c}$ and $\nu_{\rm m}$, multiple spectral regimes are possible, which in turn govern the overall shape of the light curve as shown in Granot & Sari (2002, fig. 1). The temporal evolution of these frequencies along with the peak flux $F_{\nu,\,\rm max}$ determines the shape of the light curve. We first discuss the evolution of the afterglow, followed by calculation of these quantities after a detailed analysis in Section 4.2.

4.1 Afterglow evolution

The optical light curve of GRB 210204A shows typical afterglow behaviour – a power-law decline that steepens at some point. The light curve is most densely sampled in the *r* and *R* bands; hence we use them for a first-cut analysis. Fitting a power-law to data from these bands from ∼1.4 to 8 d after the burst, we obtain indices $\alpha_r = 1.16 \pm 0.05$ and $\alpha_R = 1.17 \pm 0.04$. The fits are consistent with a constant offset in the two light curves, with $m_R = m_r - 0.24 \pm 0.03$. For the rest of the analysis, we scale the *R* band data to the *r* band by applying this offset to create a joint $r + R$ light curve.

The common light curve was used to fit a smoothly joined broken power law (Laskar et al. 2015) using the formula,

$$F_\nu = F_{\rm b} \left(\frac{(t/t_{\rm b})^{-y\alpha_1} + (t/t_{\rm b})^{-y\alpha_2}}{2} \right)^{-1/y} \quad (1)$$

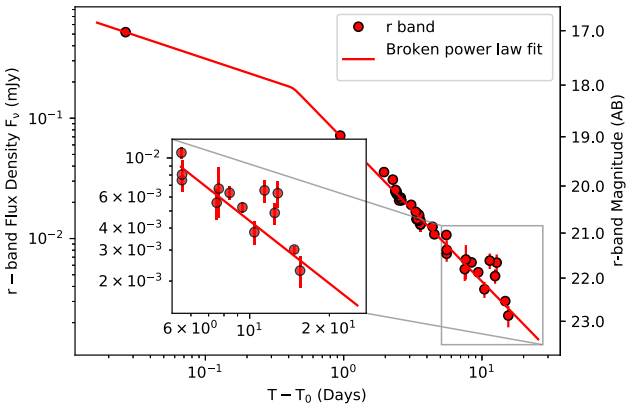

Figure 6. Broken power-law fit on r-band afterglow light curve. The red dots depicts the data points in r-band and the solid line is a broken power-law fit on the data. The inset shows a zoomed-in version of the light curve where it shows significant deviation from power-law around T − T$_0$ ∼ 10 d.

Here, F_b is flux at the break, t_b is the time since the GRB at which the break-in power law occurs, and the parameter y ensures a smooth transition between the two power-law segments. The combined $r + R$ band light curve with the broken power-law fit is shown in Fig. 6. We see a clear jet break early in the light curve, with a shallow temporal power-law index $\alpha_1 \sim 0.33$ at initial times. Due to the free smoothness parameter (y), and limited r and R data in early days ($t < 1$ d), the break time is rather poorly constrained to be $t_b = 0.37 \pm 0.30$ d (1σ error). After the jet break within the first day, the decline is steeper with a power-law index $\alpha_2 = 1.18 \pm 0.03$.

The light curve shows a significant deviation from the power-law fit at T − T$_0$ ∼ 10 d, seen clearly in the inset in Fig. 6. In order to understand these deviations, we first undertake a detailed broadband fit while excluding these days from the data in Section 4.2, and revisit the residuals in Section 4.3

4.2 Broadband afterglow modelling

We performed a detailed analysis of the multiwavelength light curve of the GRB 210204A afterglow using the AFTERGLOWPY package (Ryan et al. 2020; Ahumada et al. 2021). The AFTERGLOWPY PYTHON package is an open-source computational tool to compute the afterglow light curves for the structured jet. It has the capabilities to provide light curves for arbitrary viewing angles. We integrated the AFTERGLOWPY with EMCEE (Foreman-Mackey et al. 2013) python package for Markov Chain Monte Carlo (MCMC) routine (Metropolis et al. 1953) to generate the posterior of parameters, thanks to the fast light-curve generation of `afterglowpy`. We included all radio and X-ray data in our modelling but limited our optical data to $T - T_0 < 8$ d, in order to avoid the 'brightening' seen in Section 4.1.

We used the TopHat jet model in `afterglowpy`, which performs artificial light-curve modelling using a standard synchrotron fireball model. The temporal decay index α can be used to calculate the electron power-law index p for the circumburst medium using the closure relation $\alpha = 3(p - 1)/4$ (Table 2 Li et al. 2020). For constant density interstellar medium (ISM), the optical and X-ray decays yield $p_{\rm ISM,\,o} \sim 2.56$ and $p_{\rm ISM,\,x} \sim 2.47$. On the other hand, for a wind-like medium, $\alpha = (3p - 1)/4$, corresponding to unusually low values $p_{\rm wind,\,o} \sim 1.91$ and $p_{\rm wind,\,x} \sim 1.80$. We can also calculate that spectral index is $\beta \sim 0.75$ using the optical and X-ray fluxes, which in turn gives $p \sim 2.5$: consistent with the constant density ISM case. Hence, we proceed with detailed analysis assuming a constant density ISM.

Table 2. Posterior sampling using MCMC and `afterglowpy`.

Parameter	Unit	Prior type	Posterior	Parameter bound
$\theta_{\rm obs}$	rad	sin ($\theta_{\rm obs}$)	$0.010^{+0.002}_{-0.002}$	[0.001, 0.8]
$\log_{10}(E_0)$	erg	uniform	$54.06^{+0.03}_{-0.03}$	[48, 56]
$\theta_{\rm core}$	rad	uniform	$0.024^{+0.003}_{-0.002}$	[0.01, π/2]
$\log_{10}(n_0)$	cm^{-3}	uniform	$-5.67^{+0.13}_{-0.16}$	[−6, 100]
p	–	uniform	$2.18^{+0.026}_{-0.026}$	[2.0001, 4]
ϵ_e	–	–	0.1	–
$\log_{10}(\epsilon_B)$	–	uniform	$-0.86^{+0.17}_{-0.15}$	[−6, 0]
ξ	–	–	1	–

Assumption of constant density medium (synchrotron self absorption is not important as discussed in Section 4) may cause disagreements between the model and the radio data. However, we find that the results do not significantly change whether we include radio in the fits. The MCMC routine was run to fit for angle between the jet axis and the observer ($\theta_{\rm obs}$), the total energy of the jet ($\log_{10}(E_0)$), the half opening-angle of the jet ($\theta_{\rm core}$), the circumburst density ($\log_{10}(n_0)$), the power-law index for the electron energy distribution (p), and the fraction of energy in electrons and the magnetic field ($\log_{10}(\epsilon_e)$ and $\log_{10}(\epsilon_B)$, respectively). The priors and bounds used for each parameters are shown in Table 2. We assumed a uniform distribution for $\theta_{\rm core}$, but we took the prior for the observer angle to be uniform in $\sin\theta_{\rm obs}$ to account for the uniform random orientations of sources in space (see for instance Troja et al. 2018). The exponent p was assumed to be distributed uniformly in the semiopen interval (2, 4]: implemented practically as a uniform distribution in [2.0001, 4]. Finally, log-uniform priors were used for E_0, n_0, and ϵ_B. Our preliminary fits showed that the data could not constrain ξ and ϵ_e well, so we fixed them at nominal values of 1 (Ryan et al. 2020) and 0.1 (Panaitescu & Kumar 2002; Gupta et al. 2021a), respectively. The source redshift was held fixed at 0.876 as discussed in Section 2.2.3. Inputs for the fitting were the time since an event, observation frequency, measured flux, and the flux uncertainty. AFTERGLOWPY was used to generate models for various values of the input parameters, which were then compared to the observed data. The best-fitting parameters and the confidence intervals were evaluated by maximizing the likelihood of the model fits to the observations.

The 1D and 2D marginal posterior distribution resulted from the routine are shown in Fig. A1. For each parameter, distribution median posterior and 16 per cent and 84 per cent quantiles are plotted at the top of panel, which we also quote as the parameter bounds here. The model constrained the jet isotropic energy to be $10^{54.06 \pm 0.03}$ ergs, consistent with typical long GRB afterglows (Wu et al. 2012). The jet structure parameter ($\theta_{\rm core}$) and viewing angle ($\theta_{\rm obs}$) were constrained at $0.024^{+0.003}_{-0.002}$ rad, 0.010 ± 0.002 rad, respectively. From the values of $\theta_{\rm obs}$ and $\theta_{\rm core}$, it is evident that the jet is seen on axis ($\theta_{\rm obs} < \theta_{\rm core}$).

The best-fitting model generated from afterglow + MCMC routine fit is shown in Fig. 7. Markers denote observed flux densities, and in several cases, the error bars are smaller than the marker size. Dashed lines show the light curves in various bands, generated using median values from parameter distribution from MCMC routine. The shaded coloured bands show 16–84 per cent uncertainty regions around the median values. The fit indicates that the optical light curve would have risen at very early times, which is plausible based on the values of the synchrotron break frequencies at that time – however, we

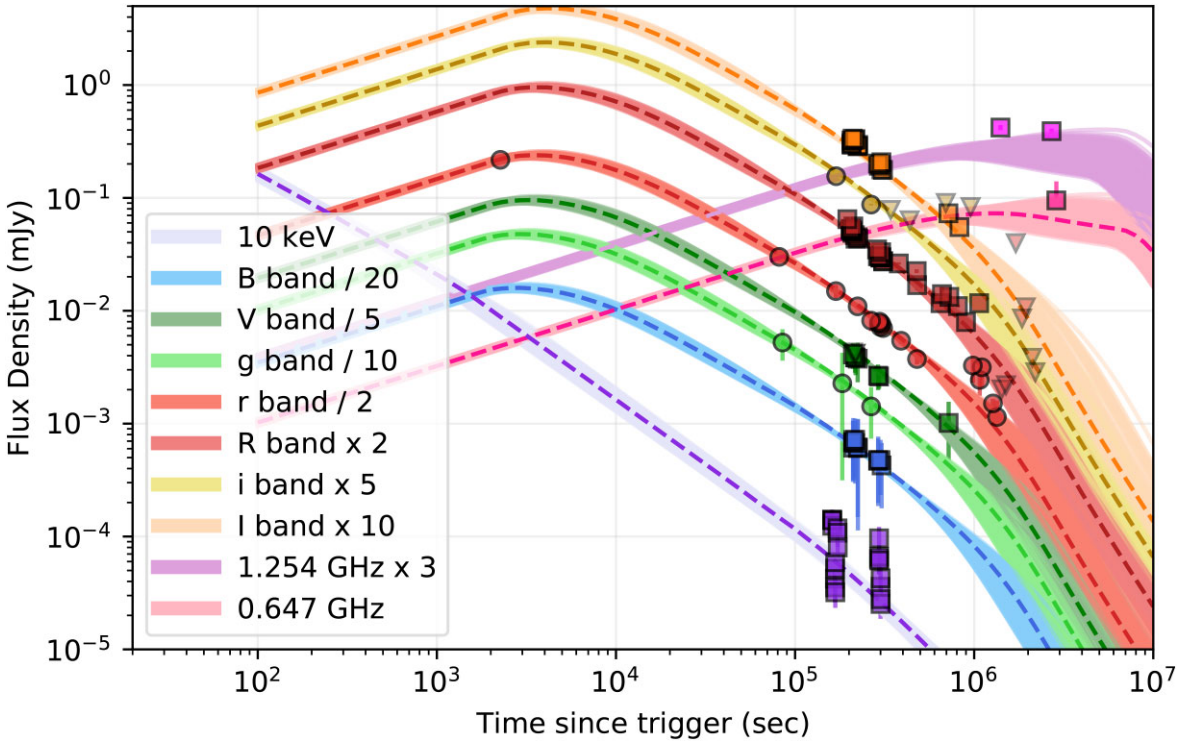

Figure 7. A multiband light curve of GRB 210204A afterglow. The multiband light curve of the GRB 210204A afterglow was fitted to the data using the AFTERGLOWPY package integrated with the AFTERGLOWPY with EMCEE PYTHON package for MCMC. Dotted lines show the best-fitting light curve to each band, and the light coloured band around the dotted line indicates the 16 per cent and 84 per cent quantiles uncertainty in the fitting.

do not have any observational data to constrain this. Note that the figure shows all data, even the points at $T - T_0 > 8$ d that were excluded from the fit. We can clearly see that the re-brightening episodes have statistically significant deviations from the fit values and are indeed astrophysical in nature.

Next, we tried to estimate the break frequencies and peak time of light curve. For this, we consider a spherical shock propagating in a constant density (n) medium. The hydrodynamic evolution of this shock can either be radiative or adiabatic, which affects the late-time light-curve behaviour. Following Sari et al. (1998), if we model the flux in a decaying part of light curve as $F \sim t^{-\beta}$, then the decay index can take two values in the adiabatic case: $\beta_1 = 3(p-1)/4$ or $\beta_2 = 3p/4 - 1/2$. Using value of p from Table 2, we get $\beta_1 = 0.88$ and $\beta_2 = 1.13$. On the other hand, $\beta \sim 3/7$ for fully radiative evolution. In Section 4.1, we measured this late-time decay index to be $\alpha_2 = 1.18 \pm 0.03$: close to the radiative β_2 calculated here. We conclude that the hydrodynamic shock evolution is adiabatic in nature. Hence, the equations governing shock parameters in the observers' frame are (Sari et al. 1998):

$$\nu_c = 2.7 \times 10^{12} * (1+z)^{-1/2} \epsilon_B^{-3/2} E_{52}^{-1/2} n_0^{-1} t_d^{-1/2} \text{ Hz} \quad (2)$$

$$\nu_m = 5.1 \times 10^{15} * (1+z)^{1/2} \left(\frac{p-2}{p-1}\right)^2 \epsilon_e^2 \epsilon_B^{1/2} E_{52}^{1/2} t_d^{-3/2} \text{ Hz} \quad (3)$$

$$t_m = 2.98 * (1+z)^{1/3} \left(\frac{p-2}{p-1}\right)^{4/3} \epsilon_e^{4/3} \epsilon_B^{1/3} E_{52}^{1/3} \nu_{15}^{-2/3} \text{ d} \quad (4)$$

$$t_0 = 1.89 \times 10^3 * (1+z) \left(\frac{p-2}{p-1}\right)^2 \epsilon_e^2 \epsilon_B^2 E_{52} n_0 \text{ d} \quad (5)$$

Here, t_d is time in days since the trigger, n_0 is the ISM density in units of cm^{-3}, $E_{52} = E_0/10^{52}$ ergs, $\nu_{15} = \nu/10^{15}$ Hz, and t_m is peak time. At $t = t_0$, equations (2) and (3) satisfy $\nu_0 = \nu_c(t_0) = \nu_m(t_0)$ (Sari et al. 1998), where ν_0 is called critical frequency. $t = t_0$ is the time at which the ejecta transitions from fast cooling to slow cooling phase. Using best–fitting values from Table 2, equation (5) yields $t_0 \sim 3.85 \times 10^{-6}$ d – showing that GRB 210204A transitioned to the slow cooling phase at very early times. This in turn gives a 'critical frequency' $\nu_0 = 2.21 \times 10^{21}$ Hz, which lies in γ – ray frequency range as shown by horizontal black-dashed line in Fig. 8, suggesting that the light curve shown in Fig. 7 is a low-frequency light curve (Sari et al. 1998). The optical light curve will peak when the synchrotron frequency (ν_m) passes through optical bands at $t_m = 0.055$ d $= 4.75 \times 10^3$ s, in agreement with the AFTERGLOWPY fits for GRB 210204A shown in Fig. 7. However, we lack sufficient early-time data to constrain such a rise. On the other hand, the cooling frequency at $\sim$1 d $\nu_{c,\,t=1} = 1.68 \times 10^{18}$ Hz, lies in X-ray bands ($E \sim 7$ keV) which accounts for different decay in X-ray and optical bands at early times.

4.3 Quantifying the re-brightening

Armed with our best-fitting model for the afterglow, we revisit the re-brightening episode discussed in Section 4.1. Fig. 6 shows that these episodes occur only for a few nights, after which the data seem to return to the original power-law decay. We verified this starting with detailed quality checks on our data in this time range: including visual inspection, checking the stability of light curves of nearby stars, and re-checking the zero points. We find that the photometric measurements are robust, and the data indeed are brighter than the level expected from the afterglow model.

Next, we fit simple models to these episodes to measure their properties. In all fits, we use the nominal afterglow light curve from Section 4.2 as a 'background' (red dashed lines in Fig. 9), and add

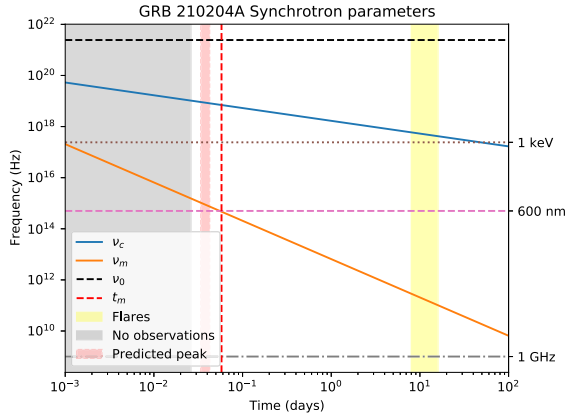

Figure 8. The interplay of break frequencies with time. The blue and orange solid line represents variation of ν_c and ν_m respectively with time. ν_m passes through the optical frequency (horizontal magenta dashed line) at $t = t_m$ (vertical dashed red line). Grey shaded region shows epochs where no observations were made. The yellow shaded region depicts flaring event. The narrow light red region at $\sim 3 \times 10^3$ s is where the light curve is predicted to be peaked through AFTERGLOWPY modelling of light curve.

various 'flare' models to this. We start with a simple Gaussian in flux density space: $F = F_0 \exp[(t - t_{\rm peak})^2/(2\sigma^2)]$, where F_0 is the peak flux density, $t_{\rm peak}$ is the time of the peak, measured from the GRB T_0, and σ is the duration parameter. We obtain best-fitting values as $F_0 = 0.0024 \pm 0.0006$ mJy, $t_{\rm peak} = (105 \pm 3) \times 10^4$ s $= 12.1 \pm 0.3$ d and $\sigma = (17.2 \pm 3.3) \times 10^4$ s $= 2.0 \pm 0.4$ d. This corresponds to an overall fluence of 7.87×10^{-10} erg cm^{-2}. However, the quality of the fit is not very good (Fig. 9a), as the photometry is close to the predicted light curve till $\sim$10 d, and rises strongly after that. Hence, we fit two gaussians to the data, as shown in Fig. 9b. The best-fitting parameters for the first peak are $F_1 = 0.002 \pm 0.011$ mJy, $t_{\rm peak,\,1} = 76 \pm 6) \times 10^4$ s $= 8.8 \pm 0.7$ d and $\sigma_1 = (3.7 \pm 1.6) \times 10^4$ s $= 0.4 \pm 0.2$ d, while the best-fitting parameters for the more pronounced second peak are $F_2 = 0.0029 \pm 0.0006$ mJy, $t_{\rm peak,\,2} = (110 \pm 3) \times 10^4$ s $= 12.7 \pm 0.3$ d and $\sigma_2 = (12.0 \pm 2) \times 10^4$ s $= 1.4 \pm 0.2$ d. The total fluence of the two peaks is 5.73×10^{-10} erg cm^{-2} and 9.83×10^{-10} erg cm^{-2}, respectively.

Any re-brightening or flaring episode is likely to have an asymmetric profile with a faster rise and slower decline that is not appropriately modelled by a Gaussian function. Hence, we fit them with a more plausible model, the Norris function (Norris et al. 2005). The intensity of the flare is modelled as

$$I(t) = A\lambda \exp\left(-\frac{\tau_1}{(t - t_i)} - \frac{(t - t_i)}{\tau_2}\right) \quad (6)$$

where t_i is the pulse start time, and the equation holds for $t > t_i$. The parameters τ_1 and τ_2 are associated with the rising and decaying phases of the pulse, but are not directly the rise and decay timescales. The burst intensity is given by the parameter $A\lambda$, where $\lambda = \exp(2\sqrt{\tau_1/\tau_2})$. We ignore the weaker first episode here, but find that the second episode is fit well by equation (6). The burst 'start time' is $t_i = 88 \pm 3 \times 10^4$. The peak time is $t_{\rm peak} = t_i + \sqrt{\tau_1/\tau_2} = (9.9 \pm 2.4) \times 10^5$ s $= 11.5 \pm 2.7$ d – consistent with, but bit sooner than, the values obtained from the double Gaussian fit. The width of the pulse is $w = \tau_2(1 + 4\sqrt{\tau_1/\tau_2}) = (3.2 \pm 1.4) \times 10^5$ s $= 3.7 \pm 1.6$ d. Under this model, the fluence of the pulse is 1.48×10^{-9} erg cm^{-2}. For comparison, the total fluence of the underlying afterglow model in the same duration is 1.85×10^{-9} erg cm^{-2}.

In summary, we see evidence for two re-brightening episodes in the afterglow, at about 8.8 and 12.7 d after the burst. The second episode is the more significant, with $\Delta t/t$ values $\sim$0.25 and 0.33, and $\Delta F/F \sim 1.14$ and 1.07 for the double-Gaussian and Norris models, respectively.

5 DISCUSSION

The afterglow of GRB 210204A is quite typical in early times, following a broken power-law behaviour (Section 4.1) that is modelled well with as a standard afterglow with AFTERGLOWPY (Section 4.2). The late-time deviations from a smooth decay (Section 4.3) can arise from a variety of reasons in long GRB afterglows.

A common cause for a re-brightening is the appearance of the supernova associated with the GRB (Section 5.1). Flaring may also occur due to patchy shells in the jet (Section 5.2) or interaction of the jet with inhomogeneities the ISM (Section 5.3). Various shocks can also cause flaring – for instance a reverse shock in the ejecta (Section 5.4) or a collision of two forward shocks (Section 5.5). Delayed activity by the central engine may manifest directly as flaring (Section 5.6), or interactions between a delayed jet and a cocoon (Section 5.7), or may refresh the forward shock (Section 5.8).

We discuss these in detail below, testing each probable cause for the re-brightening in GRB 210204A.

5.1 Supernova

In many long GRBs, the very late-time supernova (SN) bump follows the afterglow emission indicating the collapsar origin for the burst (Galama et al. 1998; de Ugarte Postigo et al. 2017; Roy 2021). To test this possibility, we used the light curve of the prototypical SN 1998bw to compare this excessive emission. As a starting point, we referred to SN 1998bw data from Clocchiatti et al. (2011) and

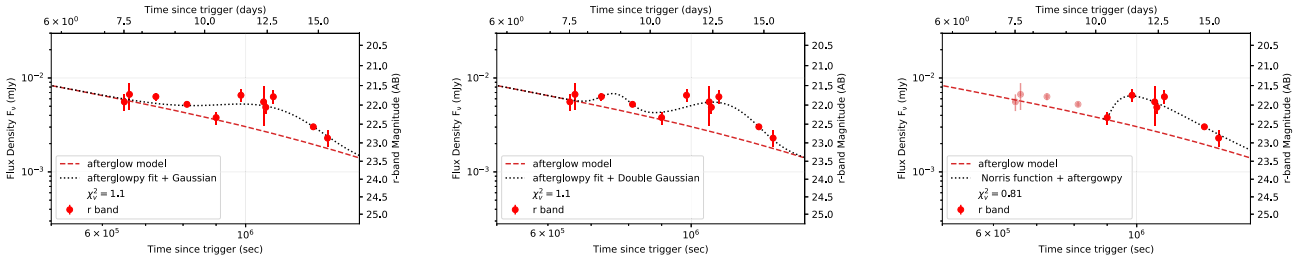

(a) 1D Gaussian fit (b) 1D Double Gaussian fit (c) Norris function fit

Figure 9. Late-time excessive emission fitting with various models. (a) A simple Gaussian fitting to the peak. (b) A double Gaussian fit to the late-time variability. (c) Norris function fitted on the two peaks for flaring. The solid dark markers shows the data used for fitting for a particular function.

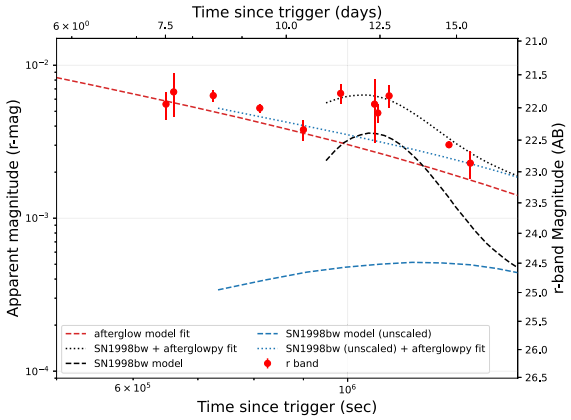

Figure 10. K-corrected SN 1998bw light curve plotted with the excessive emission in GRB 210204A. The dashed-red line shows the afterglow model, while the dotted black line shows the afterglow and scaled supernova combined model plotted in the observers' frame. The scaled supernova-only model (black-dashed line) was obtained by scaling SN 1998bw model (blue-dashed line) flux up by 7×, stretched to be eight times faster (shorter) than actual, and shifted in time such that the supernova started 6 d after the GRB. The unscaled SN 1998bw model fitted over the AFTERGLOWPY model is shown with blue-dotted lines for comparison. This is an unreasonable set of parameters; thus, a supernova cannot explain the re-brightening.

applied a *K*-correction (Bloom, Frail & Sari 2001) using redshift of GRB 210204A. Using cubic splines, we interpolated the fluxes into the observed *r* band values. A continuous light curve was created using cubic interpolation on these values. The resulted light curves were then further scaled in flux (k), stretch in evolution (s), and shifted in time (S_t) to fit GRB 210204Alight curve. The SN1988bw model light curve overplotted with the GRB 210204A data is shown in Fig. 10. Typical GRB supernovae have absolute magnitudes in the range −17.5 to −20 with median value ∼−19.5 mag (Richardson 2009), and peak about ∼20 d after the GRB in the rest frame. At the redshift of GRB 210204A, it would correspond to an apparent magnitude of 24.6, peaking 38 d after the trigger in the observers' frame. We note that this is the bolometric magnitude, while our observations are in the r band — corresponding to the rest frame u band. Thus, the expected supernova will be even fainter due to the finite bandwidth and possible extinction. The observed episodes occur much sooner and are much brighter than these values.

Thus, to explain the re-brightening seen in GRB 210204A as a supernova similar to SN 1998bw, the SNe light curve has to be made shorter by a factor of 8 ($s = 1/8$), the flux has to be made brighter by a factor of $k \sim 7$, and the supernova onset has to be delayed by ∼6 d to get a reasonable fit. These parameters – in particular the shorter time-scale and delayed onset of the supernova – are quite unphysical, and we do not find any acceptable values that can match the light curve. Hence, we conclude that the re-brightening is not associated with a supernova.

5.2 Patchy shell model

The patchy shell model attributes the variability in GRB afterglows to random angular fluctuations in the energy of the relativistic jet (Nakar & Oren 2004). However, such variations are expected at earlier times when there are causally disconnected regions within the jet opening angle. However, the variability caused by this mechanism has time-scales $\Delta t \gtrsim t$, (Nakar & Oren 2004; Ioka, Kobayashi & Zhang 2005), inconsistent with our measurements. Therefore, we rule out the patchy shell model as a potential cause for the re-brightening seen in GRB 210204A.

5.3 Variations due to fluctuation in ISM density

Ambient density fluctuations can account for late-time variability in GRB afterglows (Wang & Loeb 2000; Lazzati et al. 2002; Ioka et al. 2005). Such inhomogeneities are primarily caused due to winds from the progenitor or due to turbulence in the ambient medium. Ioka et al. (2005) put an upper limit on flux variation due to inhomogeneities in the ambient medium of standard afterglows for on-axis jets:

$$\frac{\Delta F_\nu}{F_\nu} \leq \frac{4}{5} f_c^{-1} \frac{F}{\nu F_\nu} \frac{\Delta t}{t} \tag{7}$$

Here, $f_c \sim (\nu_m/\nu_c)^{(p-2)/2}$. The light curve of GRB 210204Ais governed by slow cooling, with optical-band frequencies satisfying $\nu_m < \nu_{opt} < \nu_c$ criteria at time of excessive emission ($t \sim 12$ d) seen in GRB 210204A light curve (see Section 4.2). For such cases, the $F/\nu F_\nu \sim (\nu/\nu_m)^{(p-3)/2}$ (Ioka et al. 2005). This suggests $\frac{\Delta F_\nu}{F_\nu} \leq 0.14$, which is significantly lower than actual value of 1.07–1.14 (Section 4.3). Further, Nakar & Piran (2003) show that assuming a spherically symmetric ISM profiles, any flaring from such interactions will have $\Delta t/t > 1$, which is also inconsistent with our measurements. Thus, we rule out fluctuations in ambient density as possible origin of flare.

5.4 Reverse-shock emission in ejecta medium

The interaction of blast-wave and circumburst medium results in two shock waves: the forward shock moving towards circumburst medium and a reverse shock moving back into ejecta itself. The reverse shock could produce an optical peak in the observed optical light curve at early times (Kobayashi & Zhang 2003; Greiner et al. 2009; Gao et al. 2015). Reverse shock is expected to rise rapidly in constant density medium under thin shell approximation case ($\alpha_{rise} = 3p - 3/2$, where p is the power-law index of the electron distribution), and decline, with $\alpha_{decline} = -(27p + 7)/35$ (Kobayashi 2000; Greiner et al. 2009). The canonical range of electron distribution index (p) = 2.2 − 2.5 (Greiner et al. 2009). The estimated rising and decaying temporal indices of the optical flare are ∼6.2 and ∼3.4, respectively. This implies p ∼2.56 and 4.15 before and after the peak of the flare, respectively. The inconsistent values of p during the rising and decaying part indicate that the flare is not a result of external reverse shock decay. Moreover, the observed peak time occurs at $t_{peak} = (9.90 \pm 2.31) \times 10^5$ s post burst, far later than the 10^{3-4} s delays expected from flares caused by the reverse shock component in optical bands (Kobayashi & Zhang 2003; Uhm & Beloborodov 2007).

5.5 Collision of two forward shocks

An external collision between shells of GRB can produce flaring on top of afterglow decay (Burrows et al. 2005b; Perna, Armitage & Zhang 2006; Zhang et al. 2006; Chincarini et al. 2007). The time, amplitude, and duration of such flares vary among GRBs, depending upon the interaction time, Lorentz factor (Γ) and the energy E_{iso} of the colliding shells. Vlasis et al. (2011) discuss a scenario where a shell with a lower Γ is ejected first from the central engine, followed by a shell with a higher Γ. The first shell decelerates further as it interacts with the ISM, and the second (faster) shell can catch up and ram into the first shell, producing optical flares. For typical GRBs,

flares created by such a mechanism should have $\Delta t/t \sim 1$ where Δt is the full width at half maximum of the flare, and t is the time at which the flare peaks. We also expect $\Delta F/F \sim 2$–5, where F is the flux of the afterglow and ΔF is the excess brightening caused by the flare (Vlasis et al. 2011).

The measured $\Delta t/t$ and $\Delta F/F$ values (Section 4.3) are smaller than the predictions of Vlasis et al. (2011). Thus, we conclude that it is unlikely that collisions between forward shocks caused the late-time flaring.

5.6 Late-time flaring emission from central engine

Flaring activity is fairly common in GRB afterglows – seen in more than 50 per cent of the GRBs in X-rays (O'Brien et al. 2006) and $\sim$ 33 per cent of GRB light curves in optical (Swenson et al. 2013). Due to the very limited amount of X-ray data for GRB 210204A, we focus on r-band optical observations here – in particular, the second re-brightening episode. Flaring in afterglows may be caused by external shocks caused when the jet interacts with density bumps in the ISM (which is discussed in Section 5.3), or internal shocks from a central engine that is still active, which we discuss here. Indeed, the presence of the three episodes in the prompt emission of GRB 210204Ais itself an encouraging sign that the central engine is capable of injecting energy multiple times. Such central engine activity itself is typically ascribed to two scenarios. The first possibility is a long-lived magnetar, active to late times (Usov 1994; Dai & Lu 1998; Rees & Mészáros 2000). The other possibility is the delayed formation of a black hole in a collapsar, with an accretion disc that may feed matter to the black hole for days (MacFadyen, Woosley & Heger 2001).

Flares are typically characterized by the flaring time-scale as compared to the delay time and the fractional increase in flux (Ioka et al. 2005). From Section 4.3, we have $\Delta t/t \sim 0.25$ and $\Delta F/F \sim 1.14$. These values are consistent with the classical flaring criteria $\Delta t/t \leq 1$ (Swenson et al. 2013; Swenson & Roming 2014). Next, we compare the properties of the flare with the Swenson et al. (2013) sample. Fig. 11a shows that the flare is similar to other flares in the duration and flux ratios. What sets it apart is the peak time (Figs 11c). However, this may be an observational bias, as late-time observations by UVOT or other telescopes are not as common.

Based on the long delay after the GRB, the flares are unlikely to be directly associated with late-time central engine activity. However, we cannot fully rule out this possibility due to the lack of multiwavelength data.

5.7 Interaction of a delayed jet with a cocoon

The passage of the prompt jet through the stellar envelope creates a cocoon of material (Nakar & Piran 2017). As the main jet subsides, the cocoon quickly gets filled in due to transverse spreading, presenting a barrier to any delayed jet components like ones discussed in Section 5.6. Shen, Kumar & Piran (2010) argue that the interaction of such late jet components with the ejecta can cause broadband flaring. Such flares have $\Delta t/t < 0.5$, and the flux can vary drastically depending on the system parameters. For instance, they predict that for a GRB with redshift 2, the optical V-band magnitude for such a flare may be anywhere between 11.5 and 29, comfortably encompassing the values observed for our $z = 0.876$ case. However, the resultant flares are expected to occur at earlier times: typically starting at 100 s after the burst, but possibly up to 10^4–10^5 s after the event. The flaring in GRB 210204A occurs an order of magnitude later in time, and thus is not any more likely to be caused by interactions between a delayed jet and a cocoon than any other causes of late engine activity discussed in Section 5.6.

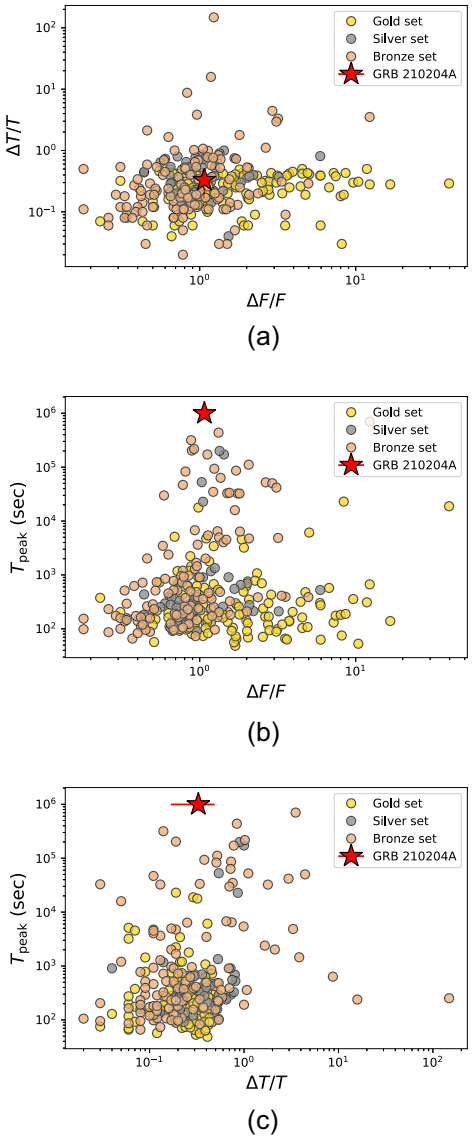

Figure 11. Comparison of flaring properties of GRB210204A with GRB flares published in Swenson & Roming (2014). The gold, silver, and bronze sets are shown by respective colors. GRB 210204A is depicted with a red star symbol, with the limits of the error bar, indicating the two Δt values measured in Section 4.3. The flare is very similar to other flares in terms of $\Delta F/F$ and $\Delta t/t$, but occurs later than any of the flares in the Swenson & Roming (2014) data set.

5.8 Refreshed shock

The late-time brightening in the optical light curve could also have originated from a forward shock that is refreshed by late-time energy injection from the central engine (Panaitescu, Mészáros & Rees 1998; Rees & Mészáros 1998). Such a refreshed shock scenario has been used to explain the observed re-brightening in the optical light curves of GRB 030329 (Granot, Nakar & Piran 2003) and GRB 120326A (Melandri et al. 2014). Consider a standard forward shock model where the bulk Lorentz factor of the ejecta is not constant but has a range of values. Faster moving shells with higher Lorentz factors

($\Gamma_{\rm fast} \geq 100$) interact with the surrounding medium first and are slowed down. Slower moving shells ($\Gamma_{\rm slow} \sim 10$) catch up with these decelerated shells at late times, injecting energy into the shock and increasing the emission. Genet, Daigne & Mochkovitch (2006) derived the formula for the collision time of two shells (one moving with $\Gamma_{\rm slow} \sim 10$ and other moving with $\Gamma_{\rm fast} \geq 100$) considering the simple assumption (see equation 8),

$$t_{\rm shock} \approx 1.66 \times E_{\gamma,{\rm iso},53}^{1/3}\, n_0^{-1/3}\, \Gamma_{{\rm slow},10}^{-8/3} \quad {\rm d} \tag{8}$$

In this equation, $E_{\gamma,\,{\rm iso},\,53}$ denotes $E_{\gamma,\,{\rm iso}}/10^{53}$ in erg, n_0 is the density for a constant medium which we obtained from broadband afterglow modelling, $\Gamma_{{\rm slow},\,10}$ is the bulk Lorentz factor of slow moving shell in the unit of 10. Following the above equation, we calculated the Lorentz factor of the slow moving shell for GRB 210204A at the time of optical brightening. We take $t_{\rm shock} \sim 12.7$ d from our two-Gaussian fit (Section 4.3), and substitute $E_{\gamma,\,{\rm iso},\,53} = 10^{1.06}$ erg, $n_0 = 10^{-5.65}$ cm^{-3} from Table 2 to get $\Gamma_{\rm slow} \sim 32$.

For flares caused by refreshed shocks, we expect $\Delta t/t > 1/4$, broadly consistent with the values measured in Section 4.3. Thus, a refreshed shock scenario is a plausible explanation for these flares.

6 SUMMARY AND CONCLUSION

We presented a detailed analysis of the prompt emission and afterglow of GRB 210204A. The prompt emission consists of three distinct emission episodes in *Fermi*-GBM data, separated by quiescent phases. Spectral analysis of the third and brightest episode shows the presence of a thermal component at low energies, adding a member to the small but growing class of GRBs with thermal components. We also find that GRB 210204A (full interval), as well as the individual pulses, are consistent with the Amati relation.

GRB 210204A stands out by having the most delayed flaring activity ever detected in GRBs. A flare is detected 8.8 d after the burst, followed by a stronger flare at 12.7 d. We analyse a multitude of possible causes for such flaring and rule out most of them. We conclude that the flaring is likely caused by late-time activity in the central engine – manifesting either as flares caused due to internal shocks, the interaction of a delayed jet with a cocoon or by refreshing a forward shock.

Such late-time data are not available for most GRBs. It is plausible that more GRBs exhibit such late-time flaring activity, but the sample suffers severally from observational biases. This underscores the need for a systematic follow-up program for GRB afterglows. We have undertaken such a program with the GIT to probe afterglow features in detail.

ACKNOWLEDGEMENTS

This work made use of data from the *GROWTH-India Telescope* (GIT) set up by the Indian Institute of Astrophysics (IIA) and the Indian Institute of Technology Bombay (IITB). It is located at the Indian Astronomical Observatory (Hanle), operated by IIA. We acknowledge funding by the IITB alumni batch of 1994, which partially supports operations of the telescope. Telescope technical details are available at https://sites.google.com/view/growthindia/.

This work is partially based on data obtained with the 2m Himalayan Chandra Telescope of the Indian Astronomical Observatory (IAO), operated by the Indian Institute of Astrophysics (IIA), an autonomous Institute under Department of Science and Technology, Government of India. We thank the staff at IAO and at IIA's Centre for Research and Education in Science and Technology (CREST) for their support.

We thank Jesper Sollerman for his useful suggestions that helped in improving quality of this work.

This research is partially based on observations (proposal number DOT-2021-C1-P62 and DOT-2021-C1-P19) obtained at the 3.6m Devasthal Optical Telescope (DOT), which is a National Facility run and managed by Aryabhatta Research Institute of Observational Sciences (ARIES), an autonomous Institute under Department of Science and Technology, Government of India.

PC acknowledges support of the Department of Atomic Energy, Government of India, under project no. 12-R&D-TFR-5.02-0700. We thank the staff of the GMRT that made these observations possible. The GMRT is run by the National Centre for Radio Astrophysics of the Tata Institute of Fundamental Research.

HK thanks the LSSTC Data Science Fellowship Program, which is funded by LSSTC, NSF Cybertraining Grant #1829740, the Brinson Foundation, and the Moore Foundation; his participation in the program has benefited this work.

RG, AA, VB, KM, and SBP acknowledge BRICS grant DST/IMRCD/BRICS /PilotCall1 /ProFCheap/2017(G) for the financial support. RG, VB, and SBP also acknowledge the financial support of Indian Space Research Organisation (ISRO) under AstroSat archival Data utilization program (DS_2B-13013(2)/1/2021-Sec.2). RG is also thankful to Dr P. Veres for sharing data files presented in Fig. 4. This publication uses data from the AstroSat mission of the ISRO\, archived at the Indian Space Science Data Centre (ISSDC).

This research has made use of data obtained from *Himalayan Chandra Telescope* under proposal number HCT-2021-C1-P02. We thank both HCT stuff for undertaking the observations. HCT observations were carried out under the ToO program.

This research has made use of the NASA/IPAC Extragalactic Database (NED), which is funded by the National Aeronautics and Space Administration and operated by the California Institute of Technology.

This research has made use of data obtained from the High Energy Astrophysics Science Archive Research Center (HEASARC) and the Leicester Database and Archive Service (LEDAS), provided by NASA's Goddard Space Flight Center and the Department of Physics and Astronomy, Leicester University, UK, respectively.

This research has made use of NASA's Astrophysics Data System.

This research has made use of data and/or services provided by the International Astronomical Union's Minor Planet Center.

This research has made use of the VizieR catalogue access tool, CDS, Strasbourg, France (DOI : 10.26093/cds/vizier). The original description of the VizieR service was published in 2000, A&AS 143, 23.

DATA AVAILABILITY

All data used in this article have been included in a tabular format within the article.

REFERENCES

Ahumada T. et al., 2021, Nature Astron., 5, 917
Alam S. et al., 2015, ApJS, 219, 12
Amati L., 2006, MNRAS, 372, 233
Andreoni I. et al., 2021, ApJ, 918, 63

Arnaud K. A., 1996, in Jacoby G. H., Barnes J., eds, ASP Conf. Ser. Vol. 101, Astronomical Data Analysis Software and Systems V. Astron. Soc. Pac., San Francisco, p. 17
Band D. et al., 1993, ApJ, 413, 281
Basak R., Rao A. R., 2013, MNRAS, 436, 3082
Bellm E., 2014, in Wozniak P. R., Graham M. J., Mahabal A. A., Seaman R., eds, The Third Hot-Wiring the Transient Universe Workshop. p. 27
Bertin E., 2011, in Evans I. N., Accomazzi A., Mink D. J., Rots A. H., eds, ASP Conf. Ser. Vol. 442, Astronomical Data Analysis Software and Systems XX. Astron. Soc. Pac., San Francisco, p. 435
Bertin E., Arnouts S., 1996, A&AS, 117, 393
Bertin E., Mellier Y., Radovich M., Missonnier G., Didelon P., Morin B., 2002, in Bohlender D. A., Durand D., Handley T. H., eds, ASP Conf. Ser. Vol. 281, Astronomical Data Analysis Software and Systems XI. Astron. Soc. Pac, San Francisco, p. 228
Bhalerao V. et al., 2017, J. Astrophys. Astron., 38, 31
Bloom J. S., Frail D. A., Sari R., 2001, AJ, 121, 2879
Burgess J. M., Bégué D., Greiner J., Giannios D., Bacelj A., Berlato F., 2020, Nature Astron., 4, 174
Burrows D. N. et al., 2005a, Space Sci. Rev., 120, 165
Burrows D. N. et al., 2005b, Science, 309, 1833
Chambers K. C. et al., 2016, preprint (arXiv:1612.05560)
Chand V. et al., 2020, ApJ, 898, 42
Chattopadhyay T., Vadawale S. V., Rao A. R., Sreekumar S., Bhattacharya D., 2014, Exp. Astron., 37, 555
Chattopadhyay T. et al., 2019, ApJ, 884, 123
Chincarini G. et al., 2007, ApJ, 671, 1903
Clocchiatti A., Suntzeff N. B., Covarrubias R., Candia P., 2011, AJ, 141, 163
Costa E. et al., 1997, Nature, 387, 783
Dai Z. G., Lu T., 1998, A&A, 333, L87
Daigne F., Bošnjak Ž., Dubus G., 2011, A&A, 526, A110
de Ugarte Postigo A., Thöne C., Cano Z., Kann D. A., Izzo L., Ramírez R. S., Bensch K., Sagues A., 2017, Proc. IAU, 12, 39
Derishev E. V., Kocharovsky V. V., Kocharovsky V. V., 2001, Adv. Space Res., 27, 813
Evans P. A., Swift Team, 2021, GRB Coord. Netw., 29412, 1
Evans P. A. et al., 2007, A&A, 469, 379
Evans P. A. et al., 2009, MNRAS, 397, 1177
Falcone A. D. et al., 2007, ApJ, 671, 1921
Fermi GBM Team 2021, GRB Coord. Netw., 29390, 1
Foreman-Mackey D., Hogg D. W., Lang D., Goodman J., 2013, PASP, 125, 306
Frederiks D. et al., 2021, GRB Coord. Netw., 29415, 1
Galama T. J. et al., 1998, Nature, 395, 670
Galama T. et al., 1999, 138
Gao H., Wang X.-G., Mészáros P., Zhang B., 2015, ApJ, 810, 160
Gehrels N. et al., 2004, ApJ, 611, 1005
Genet F., Daigne F., Mochkovitch R., 2006, in Holt S. S., Gehrels N., Nousek J. A., eds, AIP Conf. Ser. Vol. 836, Gamma-Ray Bursts in the Swift Era. Am. Inst. Phys., New York, p. 353
Goldstein A. et al., 2017, ApJ, 848, L14
Granot J., Sari R., 2002, ApJ, 568, 820
Granot J., Nakar E., Piran T., 2003, Nature, 426, 138
Greiner J. et al., 2009, ApJ, 693, 1912
Gupta R. et al., 2021a, preprint (arXiv:2111.11795)
Gupta R. et al., 2021b, MNRAS, 505, 4086
Gupta R. et al., 2021c, GRB Coord. Netw., 29490, 1
Gupta R. et al., 2022, MNRAS, 511, 1694
Hill J. M., 2010, Appl. Opt., 49, D115
Ho A. Y. Q. et al., 2022, preprint (arXiv:2201.12366)
Hurley K. et al., 2021, GRB Coord. Netw., 29408, 1
Ioannisiani B. K., Gambovskii G. A., Konshin V. M., 1976, Izv. Ordena Tr. Krasnogo Znameni Krymskoj Astrofiz. Obs., 55, 208
Ioka K., Kobayashi S., Zhang B., 2005, ApJ, 631, 429
Izzo L. et al., 2021, GRB Coord. Netw., 29411, 1
Kobayashi S., 2000, ApJ, 545, 807
Kobayashi S., Zhang B., 2003, ApJ, 582, L75
Kool E. et al., 2021, GRB Coord. Netw., 29405, 1
Kouveliotou C., Meegan C. A., Fishman G. J., Bhat N. P., Briggs M. S., Koshut T. M., Paciesas W. S., Pendleton G. N., 1993, ApJ, 413, L101
Kumar P., Zhang B., 2015, Phys. Rep., 561, 1
Kumar A., Pandey S. B., Singh A., Yadav R. K. S., Reddy B. K., Nanjappa N., Yadav S., Srinivasan R., 2021, preprint (arXiv:2111.13018)
Kunzweiler F., Biltzinger B., Berlato F., Greiner J., Burgess J., 2021, GRB Coord. Netw., 29391, 1
Lang D., Hogg D. W., Mierle K., Blanton M., Roweis S., 2010, AJ, 139, 1782
Laskar T., Berger E., Margutti R., Perley D., Zauderer B. A., Sari R., Fong W.-F., 2015, ApJ, 814, 1
Lazzati D., Rossi E., Covino S., Ghisellini G., Malesani D., 2002, A&A, 396, L5
Li L. et al., 2020, ApJ, 900, 176
Li C. Y. et al., 2021, GRB Coord. Netw., 29392, 1
MacFadyen A. I., Woosley S. E., Heger A., 2001, ApJ, 550, 410
MAGIC Collaboration, 2019, Nature, 575, 455
Maity B., Chandra P., 2021, ApJ, 907, 60
McCully C., Tewes M., 2019, Astrophysics Source Code Library, record ascl:1907.032
McMullin J. P., Waters B., Schiebel D., Young W., Golap K., 2007, in Shaw R. A., Hill F., Bell D. J., eds, ASP Conf. Ser. Vol. 376, Astronomical Data Analysis Software and Systems XVI. Astron. Soc. Pac., San Francisco, p. 127
Meegan C. et al., 2009, ApJ, 702, 791
Melandri A. et al., 2014, A&A, 572, A55
Mészáros P., Rees M. J., 1997, ApJ, 476, 232
Metropolis N., Rosenbluth A. W., Rosenbluth M. N., Teller A. H., Teller E., 1953, J. Chem. Phys., 21, 1087
Minaev P. Y., Pozanenko A. S., 2020, MNRAS, 492, 1919
Molotov I. et al., 2009, in Lacoste H., ed., ESA Special Publication Vol. 672, Fifth European Conference on Space Debris. p. 7
Nakar E., Oren Y., 2004, ApJ, 602, L97
Nakar E., Piran T., 2003, ApJ, 598, 400
Nakar E., Piran T., 2017, ApJ, 834, 28
Narayana Bhat P. et al., 2016, ApJS, 223, 28
Nava L. et al., 2012, MNRAS, 421, 1256
Norris J. P., Bonnell J. T., Kazanas D., Scargle J. D., Hakkila J., Giblin T. W., 2005, ApJ, 627, 324
O'Brien P. T. et al., 2006, ApJ, 647, 1213
Oganesyan G., Nava L., Ghirlanda G., Celotti A., 2018, A&A, 616, A138
Panaitescu A., Kumar P., 2002, ApJ, 571, 779
Panaitescu A., Mészáros P., Rees M. J., 1998, ApJ, 503, 314
Pandey S. B., Yadav R. K. S., Nanjappa N., Yadav S., Reddy B. K., Sahu S., Srinivasan R., 2018, Bull. Soc. R. Sci. Liege, 87, 42
Pe'er A., 2015, Adv. Astron., 2015, 907321
Pe'Er A., Ryde F., 2017, Int. J. Mod. Phys. D, 26, 1730018
Perna R., Armitage P. J., Zhang B., 2006, ApJ, 636, L29
Piran T., 2004, Rev. Mod. Phys., 76, 1143
Piran T., 2005, Rev. Mod. Phys., 76, 1143
Rees M. J., Mészáros P., 1998, ApJ, 496, L1
Rees M. J., Mészáros P., 2000, ApJ, 545, L73
Rhoads J. E., 1999, ApJ, 525, 737
Richardson D., 2009, AJ, 137, 347
Roy A., 2021, Galaxies, 9, 79
Ryan G., Eerten H. v., Piro L., Troja E., 2020, ApJ, 896, 166
Sagar R. et al., 2011, Curr. Sci., 101, 1020
Sagar R., Kumar B., Omar A., 2019, Curr. Sci., 117, 365
Sari R., Piran T., Narayan R., 1998, ApJ, 497, L17
Sari R., Piran T., Halpern J. P., 1999, ApJ, 519, L17
Sharma Y. et al., 2020, Journal of Astrophysics and Astronomy, 42
Shen R., Kumar P., Piran T., 2010, MNRAS, 403, 229
Spiegelhalter D. J., Best N. G., Carlin B. P., Van Der Linde A., 2002, J. R. Stat. Soc., 64, 583
Swenson C. A., Roming P. W. A., 2014, ApJ, 788, 30
Swenson C. A., Roming P. W. A., De Pasquale M., Oates S. R., 2013, ApJ, 774, 2
Troja E. et al., 2018, MNRAS, 478, L18
Uhm Z. L., Beloborodov A. M., 2007, ApJ, 665, L93

Usov V. V., 1994, in Fishman G. J., ed., AIP Conf. Ser. Vol. 307, Gamma-Ray Bursts. Am. Inst. Phys., New York, p. 552
Vadawale S. V., Chattopadhyay T., Rao A. R., Bhattacharya D., Bhalerao V. B., Vagshette N., Pawar P., Sreekumar S., 2015, A&A, 578, A73
Vianello G. et al., 2015, preprint (arXiv:1507.08343)
Vlasis A., van Eerten H. J., Meliani Z., Keppens R., 2011, MNRAS, 415, 279
Wang X., Loeb A., 2000, ApJ, 535, 788
Waratkar G. et al., 2021, GRB Coord. Netw., 29410, 1
Wu S.-W., Xu D., Zhang F.-W., Wei D.-M., 2012, MNRAS, 423, 2627
Yonetoku D., Murakami T., Nakamura T., Yamazaki R., Inoue A. K., Ioka K., 2004, ApJ, 609, 935
Zhang B., 2020, Nature Astron., 4, 210
Zhang B., 2021, GRB AFTERGLOW. EDP Sciences, p. 285
Zhang B., Fan Y. Z., Dyks J., Kobayashi S., Mészáros P., Burrows D. N., Nousek J. A., Gehrels N., 2006, ApJ, 642, 354

APPENDIX A: ADDITIONAL FIGURES FROM AFTERGLOW FITS

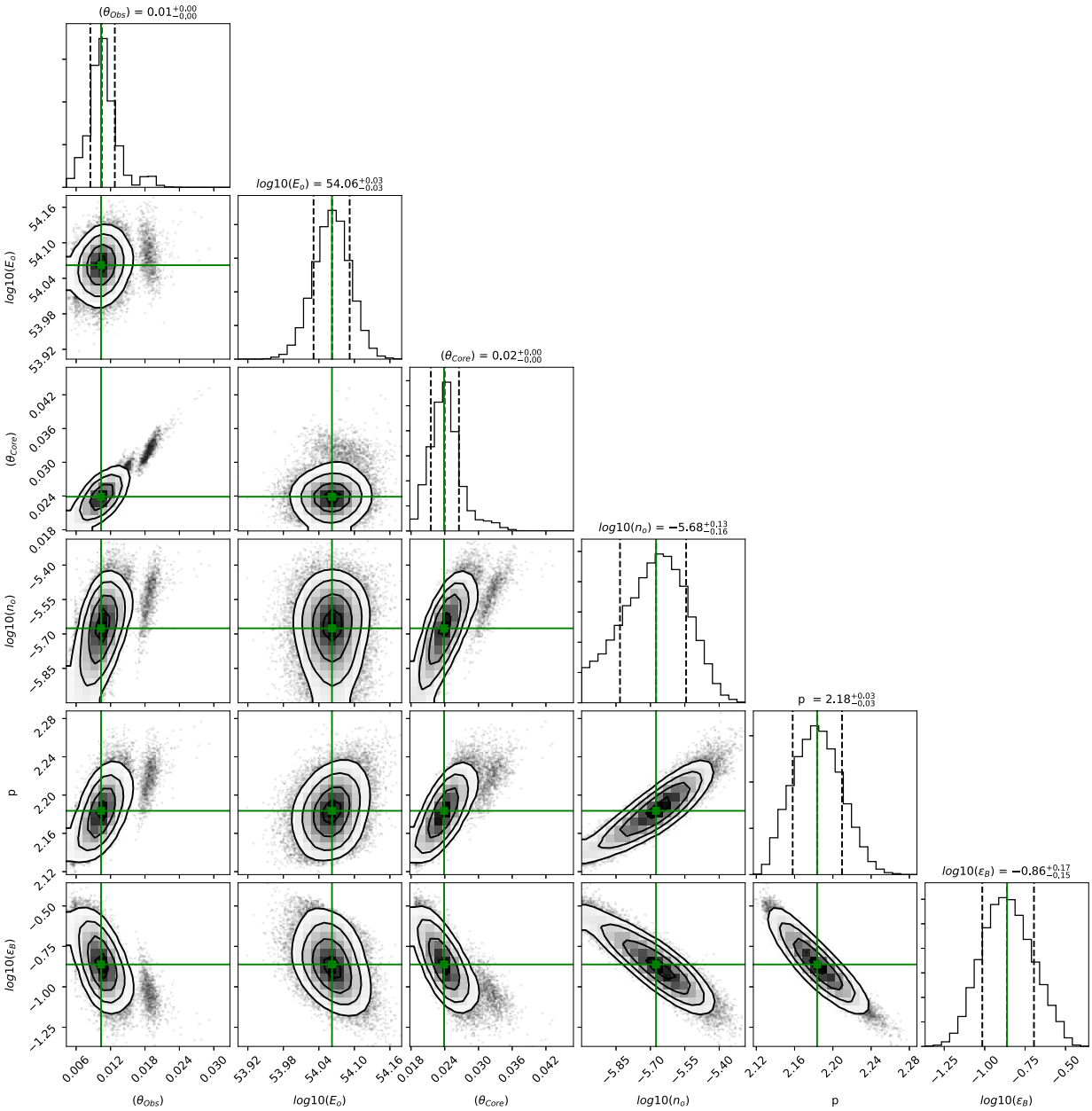

Figure A1. Posterior distribution of parameters for model fitted using AFTERGLOWPY and EMCEE. The model fit for the θ_{obs}, θ_{core}, $\log_{10}(n_0)$, p, $\log_{10}(E_0)$, $\log_{10}(\epsilon_B)$ parameters. the histogram shows the 16 per cent, 50 per cent, and 84 per cent percentiles of probability distribution.

Table A1. Log of our photometry observations of the optical afterglow of GRB 210204A, taken with various ground-based telescopes.

JD	T-T0 (s)	Filter	Magnitude	Telescope/Instrument
2459248.74875	−88273.152 00	r	>20.87	P48+ZTF
2459248.76859	−86558.155 20	g	>21.34	P48+ZTF
2459248.83259	−81029.151 36	i	>20.22	P48+ZTF
2459249.71868	−4471.148 16	g	>18.74	P48+ZTF
2459249.79662	2262.850 56	r	17.16 ± 0.03	P48+ZTF
2459250.71466	81581.852 16	r	19.31 ± 0.06	P48+ZTF
2459250.75523	85086.849 60	g	19.75 ± 0.08	P48+ZTF
2459251.72700	169047.846 72	r	19.99 ± 0.08	P48+ZTF
2459251.73331	169592.849 28	i	19.71 ± 0.10	P48+ZTF
2459251.89443	183513.850 56	g	20.62 ± 0.2	P48+ZTF
2459253.72924	342041.849 28	i	>19.80	P48+ZTF
2459254.82180	436438.851 84	i	>20.70	P48+ZTF
2459257.80761	694412.844 48	i	>20.00	P48 + ZTF
2459260.82290	954933.848 64	i	>19.70	P48+ZTF
2459252.35734	223509.456 00	r	20.55 ± 0.03	GIT
2459253.20464	296715.744 00	r	20.89 ± 0.03	GIT
2459254.29448	390877.920 00	r	21.31 ± 0.04	GIT
2459255.32039	479516.976 00	r	21.72 ± 0.05	GIT
2459266.24093	1423051.632 00	r	>22.39	GIT
2459267.194	1505396.448 00	r	>22.30	GIT
2459271.19364	1850965.344 00	r	>20.81	GIT
2459272.22723	1940267.520 00	r	>20.57	GIT
2459274.17682	2108712.096 00	r	>21.69	GIT
2459275.17860	2195266.320 00	r	>22.0	GIT
2459252.13277	204106.176 00	R	20.17 ± 0.05	HCT
2459252.13753	204517.440 00	R	20.16 ± 0.05	HCT
2459252.14045	204769.728 00	R	20.15 ± 0.03	HCT
2459252.14231	204930.432 00	R	20.20 ± 0.06	HCT
2459252.15787	206274.816 00	I	19.77 ± 0.06	HCT
2459252.16027	206482.176 00	I	19.69 ± 0.04	HCT
2459252.16265	206687.808 00	I	19.74 ± 0.06	HCT
2459252.16742	207099.936 00	I	19.78 ± 0.06	HCT
2459253.2722	302552.928 00	R	20.67 ± 0.05	HCT
2459253.28418	303588.000 00	I	20.17 ± 0.04	HCT
2459258.08132	718060.896 00	I	21.30 ± 0.20	HCT
2459258.10539	720140.544 00	V	22.14 ± 0.11	HCT
2459260.18751	900035.712 00	R	22.22 ± 0.15	HCT
2459252.18709	208799.848 22	R	20.19 ± 0.03	DFOT
2459259.15934	811201.824 00	R	21.86 ± 0.07	DFOT
2459259.34474	827220.384 00	I	21.60 ± 0.10	DFOT
2459252.18877	208944.962 21	R	20.22 ± 0.04	DOT
2459252.19235	209255.026 75	R	20.24 ± 0.04	DOT
2459252.19528	209508.051 74	I	19.64 ± 0.05	DOT
2459252.19748	209698.108 42	I	19.68 ± 0.05	DOT
2459252.20512	210359.260 22	V	20.62 ± 0.05	DOT
2459252.20909	210701.334 24	B	21.18 ± 0.09	DOT
2459252.21269	211011.890 40	B	21.30 ± 0.06	DOT
2459252.21269	211011.892 13	B	21.18 ± 0.08	DOT
2459252.21669	211357.470 53	B	21.13 ± 0.09	DOT
2459252.26456	215493.345 22	I	19.67 ± 0.04	DOT
2459252.26845	215829.424 80	R	20.29 ± 0.05	DOT
2459252.27239	216169.981 63	V	20.69 ± 0.06	DOT
2459252.27631	216509.067 07	B	21.13 ± 0.08	DOT
2459252.27990	216819.105 69	B	21.20 ± 0.09	DOT
2459252.28421	217191.691 87	I	19.66 ± 0.04	DOT
2459252.28808	217525.786 84	R	20.37 ± 0.06	DOT
2459252.29246	217903.836 09	V	20.69 ± 0.06	DOT
2459252.35158	223012.445 18	I	19.81 ± 0.07	DOT
2459252.35554	223354.019 80	R	20.34 ± 0.07	DOT
2459252.35939	223687.068 48	V	20.72 ± 0.08	DOT
2459252.36324	224019.630 72	B	21.29 ± 0.12	DOT

Table A1 – *continued*

JD	T-T0 (s)	Filter	Magnitude	Telescope/Instrument
2459252.36688	224333.718 04	B	21.31 ± 0.12	DOT
2459252.37481	225019.357 34	I	19.78 ± 0.07	DOT
2459252.37847	225335.426 69	I	19.81 ± 0.07	DOT
2459252.38265	225696.523 39	R	20.37 ± 0.08	DOT
2459253.12825	290116.631 23	R	20.76 ± 0.05	DOT
2459253.13132	290381.688 29	I	20.20 ± 0.05	DOT
2459253.13448	290654.748 58	V	21.09 ± 0.05	DOT
2459253.13721	290890.306 08	B	21.59 ± 0.09	DOT
2459253.13964	291100.846 46	B	21.57 ± 0.09	DOT
2459253.17108	293816.414 02	I	20.25 ± 0.05	DOT
2459253.17355	294030.452 74	R	20.76 ± 0.05	DOT
2459253.17646	294281.514 72	V	21.11 ± 0.05	DOT
2459253.23432	299280.583 29	I	20.22 ± 0.05	DOT
2459253.23678	299493.630 14	R	20.79 ± 0.06	DOT
2459253.23947	299725.661 66	R	20.79 ± 0.12	DOT
2459253.24264	299999.709 50	B	21.58 ± 0.08	DOT
2459253.28455	303620.974 56	I	20.33 ± 0.11	DOT
2459253.28769	303892.564 32	R	20.78 ± 0.12	DOT
2459253.29160	304230.137 76	B	21.70 ± 0.09	DOT
2459253.35684	309866.349 32	I	20.34 ± 0.07	DOT
2459253.35955	310100.869 15	R	20.88 ± 0.06	DOT
2459253.36224	310332.949 05	R	20.87 ± 0.13	DOT
2459262.54515	1103736.612 38	r	21.90 ± 0.17	DOT
2459264.50267	1272865.957 63	r	22.70 ± 0.05	DOT
2459265.27083	1339234.847 71	r	23.00 ± 0.20	DOT
2459265.43097	1353071.306 59	r	>22.59	DOT
2459266.45952	1441938.101 76	r	>21.44	DOT
2459267.38564	1521954.813 60	r	>21.13	DOT
2459269.53000	1707227.093 37	r	>19.14	DOT

Table A2. Photometry table of the optical afterglow of GRB 210204A, data obtained from various reported GCNs.

JD	T-T0 (s)	Filter	Magnitude	Instrument	Reference
2459252.0362	195 764	R	19.94 ± 0.09	AZT-33IK	29417
2459252.2179	211 462	R	20.1 ± 0.04	AS-32	29417
2459252.8472	265 835	g	21.10 ± 0.10	LBT	29433
2459252.8472	265 835	r	20.70 ± 0.10	LBT	29433
2459252.8472	265 835	i	20.40 ± 0.10	LBT	29433
2459252.8472	265 835	z	20.2 ± 0.10	LBT	29433
2459253.0930	287 073	R	20.61 ± 0.04	AZT-33IK	29438
2459254.1607	379 326	R	20.92 ± 0.05	AZT-33IK	29438
2459255.2961	477 422	R	21.09 ± 0.08	DFOT	29490
2459255.3265	480 047	R	21.4 ± 0.20	ZTSh	29499
2459257.2800	648 835	R	21.8 ± 0.20	AS-32	29499
2459257.4186	660 802	R	21.6 ± 0.30	AS-32	29499
2459258.1744	726 104	R	21.66 ± 0.09	AZT-33IK	29520
2459261.1528	983 436	r	21.86 ± 0.15	AZT-20	29520
2459262.1110	1066 228	R	21.8 ± 0.40	AZT-33IK	29520
2459262.2063	1074 461	r	22.18 ± 0.14	AZT-20	29520

Table A3. Log of X-ray observations of the X-ray afterglow of GRB 210204Ataken using *Swift*XRT in 10 keVband. This data uses a absorption of $0.61 \times 10^{22}\mathrm{cm}^{-2}$ at $z = 0.876$.

JD	T-T0 (s)	Photon Index	Flux Density (μJy)
2459251.634	161000.965	$1.61^{+0.29}_{-0.22}$	140.99 ± 31.98
2459251.636	161214.462	$1.62^{+0.28}_{-0.21}$	124.61 ± 28.42
2459251.640	161501.848	$1.65^{+0.27}_{-0.20}$	138.95 ± 24.97
2459251.702	166845.863	$2.11^{+0.24}_{-0.19}$	42.26 ± 9.79
2459251.704	167087.251	$2.13^{+0.25}_{-0.20}$	35.41 ± 9.41
2459251.706	167273.799	$2.15^{+0.25}_{-0.20}$	51.94 ± 11.80
2459251.708	167449.688	$2.14^{+0.25}_{-0.20}$	59.20 ± 13.42
2459251.712	167726.371	$2.11^{+0.24}_{-0.19}$	32.05 ± 8.73
2459251.767	172498.443	$1.64^{+0.29}_{-0.22}$	118.14 ± 26.65
2459251.769	172708.123	$1.62^{+0.30}_{-0.23}$	107.96 ± 27.21
2459251.773	173048.102	$1.61^{+0.30}_{-0.23}$	80.00 ± 17.04
2459253.174	294064.238	$1.46^{+0.30}_{-0.22}$	63.53 ± 16.86
2459253.178	294390.208	$1.46^{+0.30}_{-0.22}$	96.35 ± 25.20
2459253.182	294775.487	$1.48^{+0.29}_{-0.22}$	66.52 ± 17.42
2459253.187	295152.375	$1.52^{+0.27}_{-0.20}$	61.49 ± 15.55
2459253.239	299664.401	$2.0^{+0.29}_{-0.21}$	35.88 ± 9.36
2459253.243	300009.566	$2.04^{+0.30}_{-0.23}$	25.27 ± 6.62
2459253.247	300337.201	$2.08^{+0.32}_{-0.24}$	42.59 ± 11.11
2459253.250	300677.495	$2.11^{+0.34}_{-0.26}$	27.84 ± 7.04

Table A3 – *continued*

Table A4. Log of radio data for the radio afterglow of GRB 210204Ataken using uGMRT.

JD	T-T0 (s)	Energy-band	Flux (μJy)
2459266.06	1402272.00	1254.6 GHz	140 ± 22
2459281.09	2706011.71	1254.6 GHz	130 ± 20
2459283.06	2876272.416	647.8 GHz	95 ± 45

This paper has been typeset from a TEX/LATEX file prepared by the author.